

UNIVERSITY OF CALGARY

**Modeling and Simulation of a MEMS-Based Mass Measurement Sensor in Viscous
Environments**

by

Humud Ali Said

A THESIS

**SUBMITTED TO THE FACULTY OF GRADUATE STUDIES
IN PARTIAL FULFILLMENT OF THE REQUIREMENTS FOR THE
DEGREE OF MASTER OF SCIENCE**

DEPARTMENT OF ELECTRICAL AND COMPUTER ENGINEERING

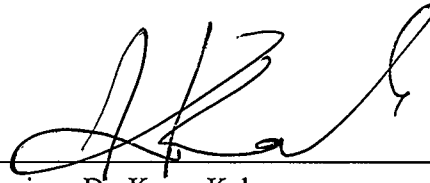
CALGARY, ALBERTA

December, 2004

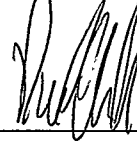
© Humud Ali Said 2004

UNIVERSITY OF CALGARY
FACULTY OF GRADUATE STUDIES


The undersigned certify that they have read, and recommend to the Faculty of Graduate Studies for acceptance, a thesis entitled "Modeling and Simulation of a MEMS-Based Mass Measurement Sensor in Viscous Environments" submitted by Humud Ali Said in partial fulfillment of the requirements for the degree of Master of Science.



Supervisor, Dr. Karan Kaler
Department of Electrical and Computer Engineering



Dr. David Westwick
Department of Electrical and Computer Engineering



Dr. Swavik Spiewak
Department of Mechanical and Manufacturing
Engineering

20th Dec, 2004.

Date

Abstract

Microelectromechanical Systems (MEMS) are devices manufactured using existing integrated circuit (IC) technologies. By using IC based technologies, designers can create micron scale mechanical devices with new capabilities as well extending the utility of integrated circuits by allowing integration of sensors, electronics and actuators on the same die. MEMS technology is now established in some industries, especially the automotive industry where pressure sensors and accelerometers have been used for more than a decade. Recently, there has been a surge of interest in biomedical applications of MEMS, also known as Bio-MEMS.

In this work, a MEMS-based precise mass sensor for biomedical applications is proposed. The mass sensor, with proper surface treatment, can be used to detect the presence of bioparticles of interest such as bacteria or viruses. The sensor is based on a micron scale cantilever beam operating in a dynamic mode. The natural frequency of the cantilever depends on its mass and therefore when the beam is loaded, the frequency shift can be used to determine how much mass was added. Electrostatic actuation is used to oscillate the cantilever to ensure that the displacement of the beam is above the thermal noise floor.

Extensive modeling and simulation of the damping phenomenon, electrostatic actuation, modal analysis and reduced order modeling are performed. It is shown that the second mode of vibration is better in terms of reduced damping and sensitivity to precise location of the mass on the beam. Finite element simulations for the different domains carried out using ANSYS and extracted reduced order model code in VHDL-AMS was generated. Parameters from the VHDL-AMS code were used in a system simulator Simulink to demonstrate the advantage of using feedback to control damping.

Acknowledgements

First and foremost, I will like to thank my supervisor Dr. Karan Kaler for providing me the opportunity to perform research aligned with my interests. His guidance, vision and technical knowledge contributed tremendously to my learning experience. Thanks to the Biosystems Research and Application Group team for a stimulating environment. I will like to thank Dr. Colin Dalton for his help in reading this thesis and providing significant constructive criticism. Thanks to Dr. Subir Bhattacharjee at University of Alberta for providing the access to the atomic force microscope used for some of the experiments. Thanks to my defense committee, Dr. Westwick and Dr. Spiewak for their time and effort in reading and making changes to the thesis.

Finally but most importantly, I would like to thank the love of my life, my partner and friend, Kim for her understanding and accommodation. Without her support, none of this would have been possible.

Dedication

*Dedicated to my grandmother Bibi Fatma Ahmed
and my parents Ali and Safia.*

Table of Contents

Approval Page	ii
Abstract	iii
Acknowledgements	iv
Dedication	v
Table of Contents	vi
1 Introduction	1
1.1 MEMS and Bio-MEMS	2
1.2 MEMS Modelling and Simulation	4
1.3 Mass Measurement by Resonating Structures	7
1.4 Thesis Outline	9
2 Analytical Background	11
2.1 Cantilever Beam Vibration	11
2.1.1 Governing Partial Differential Equation	11
2.1.2 Discretization Using Normal Coordinate Transformation	14
2.1.3 Single Degree of Freedom Equation	17
2.1.4 Resonant Frequency Approximation — Rayleigh’s Method	23
2.1.5 Resonant Frequency Shift for Mass Measurement	25
2.2 Electrostatic Actuation	26
2.2.1 Pull-In Phenomena	29
2.3 Damping	31
2.3.1 Squeeze Film Damping	32

2.3.2	Damping effect on measurement sensitivity	35
2.3.3	Practical Damping Factor Measurement	35
2.4	Quality Factor Control	38
2.4.1	Q -Control Basics	38
3	Finite Element Modeling	40
3.1	The Finite Element Method (FEM)	40
3.1.1	Direct Method	41
3.1.2	The Variational Method	43
3.1.3	The Weighted Residual Method	43
3.2	The ANSYS FEM Software	45
3.3	Electrostatic Actuation	46
3.4	Cantilever Vibration Frequency	49
3.4.1	Resonant Frequency Shift Due to Mass Change	54
3.5	Mass Placement Dependence on the Vibration Modes	57
3.6	Viscous Damping	58
3.6.1	Arbitrary Lagrangian Eulerian (ALE) Formulation	59
3.6.2	Damping Coefficient Extraction	60
4	System Level Modeling	73
4.1	Reduced Order Modeling (ROM)	73
4.2	ROM in ANSYS	74
4.2.1	The ROM144 Element	74
4.2.2	Damped Harmonic Response	76
4.3	The VHDL Language	77
4.3.1	VHDL-AMS Code	79
4.4	System Level Simulation of a Q -Controlled Sensor	80

4.5	MUMPs-Based Chip	82
4.6	Measurement Techniques	83
4.6.1	Static Measurements	83
4.6.2	Vibration Measurements	85
5	Conclusions	96
5.1	Summary of Accomplishments	96
5.2	Suggestions for Future Work	97
	Bibliography	98
A	VHDL-AMS Code Generated by ANSYS	103
A.1	Initialization File	103
A.2	Capacitance Paramaters	103
A.3	Strain Energy Parameters	104
A.4	Transducer	105

List of Tables

3.1	The resonant frequency variation with the thickness of the beam. The width was fixed at $1.5\mu\text{m}$ and the length was fixed at $5\mu\text{m}$	53
3.2	The resonant frequency variation with the length of the beam. The width was fixed at $1.5\mu\text{m}$ and the thickness was fixed at 30nm	54
3.3	The resonant frequency variation with the width of the beam. The length was fixed at $5\mu\text{m}$ and the thickness was fixed at 30nm	54

List of Figures

1.1	A general overview of a Lab-on-a-chip device.	2
1.2	SEM image of a Silicon accelerometer [1].	4
1.3	system level model of the accelerometer on the right hand side connected to feed-back and amplification electronics [1].	5
1.4	Modelling abstraction levels for different MEMS practitioners.	6
1.5	When mass of a vibrating cantilever beam changes, the resonant frequency shifts by Δf . By measuring this frequency shift, the mass of the bioparticles on the beam can be determined.	8
1.6	Decrease in the quality factor due to viscous damping produces a broader frequency response. The minimum value of Δf that can be detected is significantly reduced.	8
2.1	Uniform beam subjected to dynamic loading per unit length p	12
2.2	Forces and moments acting on a differential element dx	12
2.3	A typical underdamped response.	21
2.4	Variation of D with normalized frequency for different values of damping ratio. . .	24
2.5	A conducting cantilever beam suspended on top of the ground plane is electrically equivalent to a capacitor C	27
2.6	Electrostatic force F_e is from the opposite charges $+q$ and $-q$ built on the plates by the voltage source V	27
2.7	A column of fluid between two plates.	32
2.8	Top view of a chain of plates representing a cantilever beam.	33
2.9	Frequency response curve obtained by sweeping the input force at different frequencies.	36
2.10	Setup used for Q control implementation expressed by Equation 2.112.	39

3.1	A plane structure of arbitrary shape shown on the left is discretized into simple finite elements shown on the right.	41
3.2	A summary of different FEM techniques with their advantages and disadvantages. .	44
3.3	SOLID45 brick elements represent the structural domain while SOLID123 tetrahedral element represent the electrostatic domain.	46
3.4	Beam deformation when 100V is applied to the cantilever beam with respect to the ground plane.	48
3.5	The comparison between the analytical and FEM results for the beam displacement as a function of the voltage.	48
3.6	The comparison between the analytical and FEM results for the beam displacement as a function of the square of the applied voltage. The curves shows a linear relationship as expected.	49
3.7	The relationship between the modal response and the harmonic response for a tuning fork. Adapted from [2].	50
3.8	A cantilever beam modelled in ANSYS.	51
3.9	A cantilever beam meshed using SOLID95 elements. The nodes on the left hand side were fixed and a distributed pressure was applied on the top surface of the beam to represent the distributed electrostatic force.	51
3.10	The first mode of vibration.	52
3.11	The second mode of vibration.	52
3.12	Harmonic analysis performed in ANSYS at two different points on the beam. . . .	55
3.13	The cantilever beam with a mass loaded at the free end. The beam used had the dimensions of $L = 40\mu\text{m}$, $T = 1\mu\text{m}$ and $w = 2\mu\text{m}$	55
3.14	Comparison between the ANSYS simulation for the effect of mass loading on the first mode resonant frequency and the analytical expression given by Equation 2.65 from Chapter 2.	56

3.15	Comparison between the ANSYS simulation for the effect of mass loading on the second mode resonant frequency and the analytical expression given by Equation 2.66 from Chapter 2.	56
3.16	One dimensional illustration of the Lagrangian description of motion. The mesh moves with the body [3].	59
3.17	One dimensional illustration of the Eulerian description of motion. The mesh is stationary relative to the body [3].	60
3.18	An oscillating beam experiencing fluid force from the surrounding fluid.	61
3.19	Plot of the beam displacement and the fluid pressure used to determine the phase difference φ	63
3.20	FLUID136 nodes on top of SOLID45 nodes. The nodes have to coincide at the boundary.	64
3.21	The FLUID136 element excited using the first mode shape.	65
3.22	The FLUID136 element excited using the second mode shape.	65
3.23	The damping ratio as calculated by an analytical approximation based on simplified Reynold's equation compared to the value calculated by ANSYS. The horizontal axis represents the cantilever resonance frequency. The beam simulated has the width of $2\mu\text{m}$, length of $40\mu\text{m}$ and thickness of $1\mu\text{m}$	67
3.24	Comparison between the analytical and ANSYS results for the damping ratio for a beam that is $10\mu\text{m}$ wide with other dimensions as the beam in Figure 3.23.	68
3.25	Comparison between the analytical and ANSYS results for the damping ratio for a beam as a function of the gap.	68
3.26	Comparison between the analytical and ANSYS results for the damping ratio for a beam for the second mode. The dimensions used are the same as those for Figure 3.23.	69

3.27	The analytical Reynold's equation assumes rigid body deformation as shown on the right. The actual displacement is as shown on the right for the first mode covering less area between the moving surface and the fluid. Hence, the actual damping is less than the one predicted by the analytical Reynold's equation.	69
3.28	The damping ratio plotted with stiffness ratio as a function of frequency. The stiffness ratio describes how much the fluidic stiffness contributes to the overall structural stiffness. In this case, at resonance we have a ratio of roughly 0.05 which means the fluidic stiffness adds an extra 5% to the structural stiffness.	70
3.29	The effect of fluid viscosity on the damping ratio and fluid stiffness as a function of frequency.	71
4.1	The ROM144 generation process.	75
4.2	The damped harmonic response using full FEM harmonic analysis.	77
4.3	The damped harmonic response using the ROM. The ROM was used within the ANSYS environment.	78
4.4	General outline of VHDL code.	79
4.5	The second order system representing the cantilever beam dynamics.	80
4.6	Feedback control used to reduce damping.	82
4.7	Comparison between the uncontrolled and feedback controlled frequency responses.	83
4.8	Comparison between the uncontrolled and feedback controlled frequency responses using analytical expression of the modified transfer function.	84
4.9	An SEM image of an array of cantilever beams fabricated in MUMPs process.	84
4.10	An SEM image of side view of one of the cantilever beams.	85
4.11	A profilometer image of the cantilever beam with no voltage applied.	86
4.12	A profilometer image of the shattered cantilever beam. The pull-in voltage was found to be around 42V.	87
4.13	Comparison between measured and ANSYS results for electrostatic actuation.	88

4.14	A bump close to the fixed end of the beam results in a lower stiffness.	89
4.15	A capacitor divider for displacement measurement.	89
4.16	The AFM tip track the motion of the sensor cantilever with the displacement detected by a position sensitive photodetector.	91
4.17	Measured results using the Nanoscope III AFM. No output was observed at any frequency other than the resonant frequency of the AFM cantilever indicating strong coupling between the vibrations. The larger amplitude is clipped at the bottom because the AFM cantilever hits on the sensor cantilever.	92
4.18	Schematic of the interferometer setup to measure vibrations of the MEMS cantilever beam.	95

Nomenclature

δ	Fluid viscosity.
ϵ	Electrical permittivity.
γ	Young's Modulus of the cantilever beam.
ω_d	Damped radial resonant frequency.
ω_o	Radial resonant frequency.
Φ_n	n th mode shape function in modal decomposition analysis. This is a spatial basis function.
\Re	Frequency responsivity to added mass.
ρ	Fluid density.
ξ	Damping ratio.
C	Electrical capacitance.
c	Damping factor of an oscillating cantilever beam.
c^*	Effective damping factor of an oscillating cantilever beam modified by the feedback loop.
c_c	Critical damping factor.
D	Dynamic magnification factor.
F	External force applied on the cantilever beam.
f_o	Resonant frequency.
G	Gain of the feedback amplifier used for Q control.
g	Gap between the cantilever beam and the ground plane.

I	Moment of inertia.
k	Cantilever beam stiffness.
$K.E$	Kinetic energy.
L	Length of the cantilever beam.
M	Moment.
m	Mass of the cantilever beam.
P	Fluid pressure.
$P.E$	Potential energy.
Q	Quality factor of a harmonic oscillator.
q	Electrical charge.
T	Thickness of the cantilever beam.
V	Electrical potential difference.
W	Energy.
w	Width of the cantilever beam.
W^*	Co-energy.
Y_n	n th Mode amplitude in modal decomposition analysis. This is a temporal function.

Chapter 1

Introduction

Recently, there has been a growing interest in the implementation of integrated sampling, analysis, and detection of biological particles, also known as *Lab-on-a-chip*. The idea is to integrate and automate all or most of the tasks conventionally performed by different people and equipment in a biological laboratory. This integration will have a significant impact on the productivity of biomedical practitioners by reducing the time required to process samples [4]. On top of integration and automation, miniaturization using batch fabrication techniques will also reduce the cost of devices allowing disposable devices to be more practical [4] [5].

Figure 1.1 shows a general overview of a Lab-on-a-chip [4] which generally consists of different ports for insertion of samples, buffers, and reagents [6] [7]. The first port is for sample injection. After mixing the sample with the required buffers and reagents, the result is collected in the sample channel where there is a relatively large chamber. Several sensing or diagnostic tests can be performed in this chamber depending on the sample. Once sensing is done, the sample can be separated using a separation buffer for further processing. Even though Figure 1.1 illustrates the mixing and separation done chemically (by using buffers), these tasks can also be performed by other means such as microfluidic or electrostatic based.

Much research is going on in different aspects of separation and sensing. Electrokinetics techniques, whereby alternating electric fields are used to manipulate biological particles, are well established in terms of separation because different biological particles have different electric field responses [8]. Sensing techniques can be implemented in a variety of domains including chemical, optical, electrical, biological, and mechanical [9]. For detection, optical and electrical probing can be used to identify a bioparticle of interest which has a unique optical or electrical response,

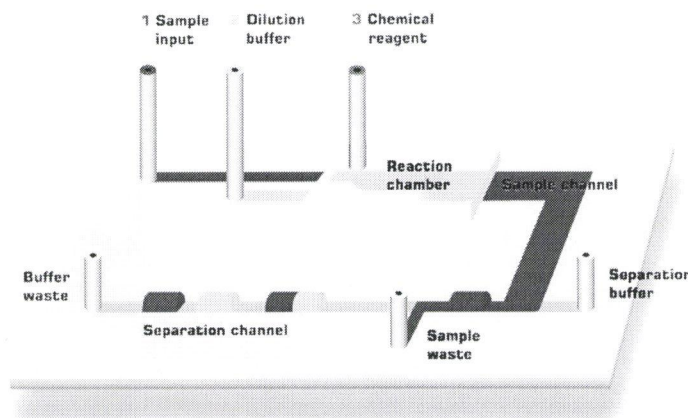


Figure 1.1: A general overview of a Lab-on-a-chip device.

respectively. Alternatively, by combining chemical selectivity and mechanical characteristics of structures, very sensitive detection methods can be implemented. An area of sensor design with a lot of potential is the microelectromechanical systems (MEMS) area and, more recently, nano-electromechanical systems (NEMS) [10]. The following section gives an overview of the MEMS field and also describes the more specific area of biomedical MEMS, more commonly known as Bio-MEMS.

1.1 MEMS and Bio-MEMS

Originally, the term MEMS represented systems which integrate mechanical and electrical components at the micron scale. However, more recently, all micron scale systems that are not purely electrical are called MEMS. Many physical domains have been explored, including fluidic, thermal, optical, and magnetic. Even though *microsystems* may be a more appropriate term, MEMS has stuck in the academic as well as industrial literature, especially in North America.

MEMS are made by using modified integrated circuit (IC) manufacturing techniques. These techniques allow for large economies of scale for volume manufacturing — a phenomenon which has led to the proliferation of microelectronics. Another advantage of using IC-based fabrication techniques is the ability to integrate the non-electrical portions of the system to the electronics re-

quired for signal processing. Being able to create miniature transducers with electronics integrated on the same chip allows for a much more dynamic range in our measurement abilities. The smaller sensors are able to detect much smaller signals, while the integrated electronics reduce the stray noise usually associated with long interconnects.

There are two main ways of manufacturing MEMS, even though the differences are becoming blurry because of advances in the fabrication techniques. The first method is known as *bulk micromachining* [11]. In bulk micromachining, the process starts with a Silicon wafer and the structures are made by etching into the wafer. This process has the advantage of being able to create relatively large structures, which are sometimes needed to overcome thermal noise. However, the designer is limited in the shape of the structures that can be made. The alternative technique is known as *surface micromachining* [12]. In this method, the substrate is used only as a platform and thin films of other materials are deposited on top of it. The thickness of the film is limited; hence, the structures that can be made are smaller than those made using bulk micromachining. On the positive side, this technique is easier to integrate with IC fabrication.

MEMS is well established in some industries especially in the automotive industry with products like pressure sensors used in car tires and accelerometers used for airbag deployment. More lately, research in Bio-MEMS has gained a lot of attention. A variety of micron scale devices for *in vitro* and *in vivo* applications have been developed [13]. The majority of these applications are sensors with some actuators used for blood sampling, drug delivery, and micro surgery. Bio-MEMS brings out unique challenges especially in packaging and operation of dynamic sensors because the environments are usually fluidic in nature. This environment requires novel materials to be used to increase the sensors' reliability and also novel system level techniques to ensure the operation of dynamic sensors does not suffer because of the environment. To allow for proper system level design, modeling techniques are required to provide the link between the purely mechanical devices and the rest of the system. MEMS modeling techniques is an intensive research area, and the following section provides a brief overview of the modeling techniques and the challenges that

come with them.

1.2 MEMS Modelling and Simulation

As mentioned previously, MEMS manufacturing techniques have been advancing rapidly. With this advance, there have been new devices, applications, and markets. However, the MEMS design tools have not been able to advance at the same pace because of the complexity in modelling MEMS devices [1], [14]. Since by definition MEMS devices involve more than one physical domain, it is very complex to develop accurate mathematical models that can be easily used by a system level designer. To demonstrate the importance of system level models, consider Figure 1.2 which shows a die of a microfabricated silicon accelerometer [1]. The device designers created mask layouts that were then passed on to process engineers who converted the mask designs into a fabricated mechanical structure.

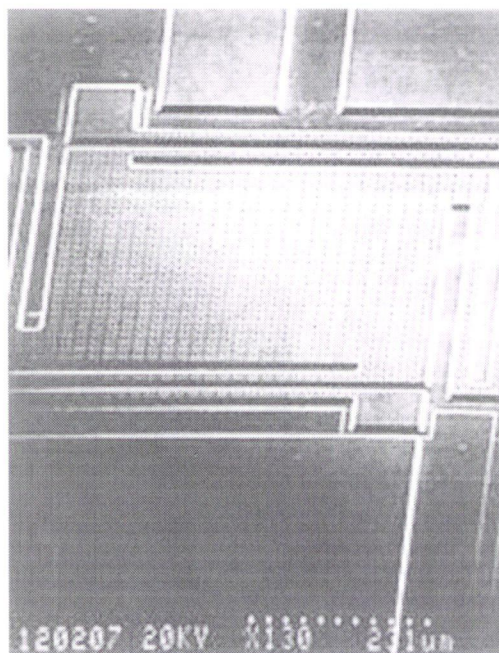


Figure 1.2: SEM image of a Silicon accelerometer [1].

The stand-alone mechanical structure as shown is not very useful because conditioning and signal processing circuits are required to properly extract the acceleration signal and to control the mechanical structure using feedback techniques. To design the overall system properly, a system designer needs a model that accurately represents the device that can be inserted into a system level simulator and connected to other system elements as shown in Figure 1.3.

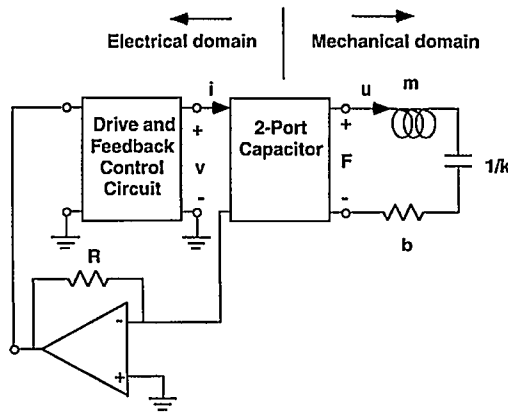


Figure 1.3: system level model of the accelerometer on the right hand side connected to feedback and amplification electronics [1].

To get a better perspective on the modeling aspect of MEMS, it is useful to compare it to the hierarchical IC design. For IC design, different practitioners view the system at different abstraction levels. For example, a digital systems designer deals with pre-built libraries of digital components such as adders and multipliers. A digital circuit designer builds the adders and multipliers using lower level digital circuits like gates and flip-flops. An analog circuit designer is needed to work at the transistor level to design the gates; finally a solid state physicist works at the device level designing and optimizing transistors. At the bottom of this hierarchy, a process engineer is required to design the fabrication process and do mask design. The biggest factor in the proliferation of microelectronics is the development of modeling tools so that the designers at the system level (digital system designer in this case) do not have to worry about the lower level functioning of the

system components. With MEMS, significant efforts have been devoted to mimic this hierarchical design structure, but the existing tools have a long way to go.

Figure 1.4 shows the equivalent hierarchy for MEMS design [1]. At the process level, the process engineer uses technology specific simulators (TCAD) to design and optimize the process flow. The process information is then used to generate three-dimensional models of the structures to be built. These 3-D models are inserted into 3-D simulators which generally solve partial differential equations (PDE) governing the physical phenomena of interest. Different techniques exist to use the output of the 3-D simulators to generate macro-models or reduced order models (ROM). Ideally, ROMs are accurate representations of the 3-D models but with very few degrees of freedom. The use of ROMs enables complex simulations to be performed without the need for huge computational resources that a fully fledged 3-D simulation will require. Finally, ROMs can be inserted into system level simulators for complete system design and optimization. For maximum productivity, these different levels have to be used by different engineers with easy interfacing between them. Most MEMS designers today have to move up and down the hierarchy and concern themselves with different aspects of the system, components, device, and process issues. This makes the design process very costly as each new MEMS design has to start from scratch.

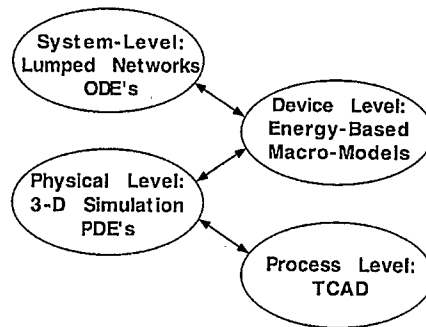


Figure 1.4: Modelling abstraction levels for different MEMS practitioners.

This research focuses on extracting ROMs from a 3-D model representing multiple physical domains. The designed structure is a dynamic cantilever beam for precise mass measurement of micro-scale to nano-scale objects. Electrostatic actuation is used to drive the cantilever, which is immersed in a viscous fluid. The modeling requires coupling of electrostatic and structural domains for the actuation, and structural and fluidic domains for the viscous damping of the cantilever beam. The extracted ROMs are compared to first-order analytical approximations, which are described in Chapter 2. Then, the ROMs are used in a system level simulator to design an enhanced sensor with increased mass measurement sensitivity. The following section gives a detailed overview of the mass measurement device.

1.3 Mass Measurement by Resonating Structures

Resonant cantilever beam structures are one of the simplest structures that can be fabricated with Microelectromechanical Systems (MEMS) or Nanoelectromechanical Systems (NEMS) technology, and they have been used for different sensing applications [15] [10]. The dynamic cantilever parameters (frequency or amplitude) can be modulated by a signal of interest. The sensitivity of these sensors depends on the size of the cantilever beam and the resolution of the parameter being measured (for example, the resolution of frequency change discrimination for frequency modulated sensors as shown in Figure 1.5). Precise mass measurement has been studied using resonant MEMS cantilever beams, but the resolution drops dramatically once the beams are in viscous fluidic environments [16] [17]. Viscosity has a big impact on the quality (Q) factor of the resonating cantilever beam. The smaller the Q factor, the broader the frequency response as shown in Figure 1.6. It is apparent that this reduction in Q factor results in lower frequency shift discrimination. Hence, this mass measurement method has been demonstrated successfully only in air or vacuums [18] [19].

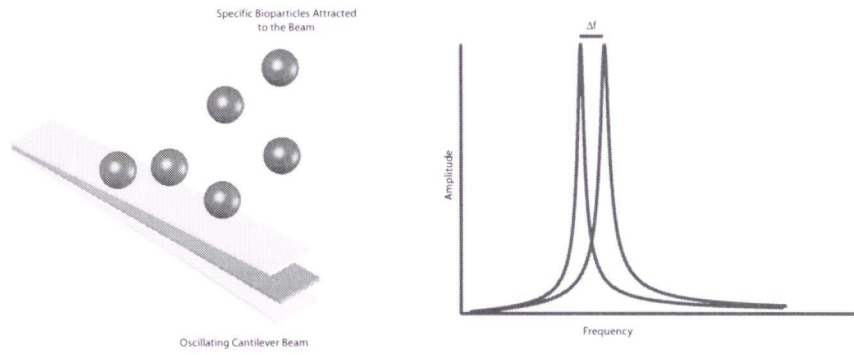


Figure 1.5: When mass of a vibrating cantilever beam changes, the resonant frequency shifts by Δf . By measuring this frequency shift, the mass of the bioparticles on the beam can be determined.

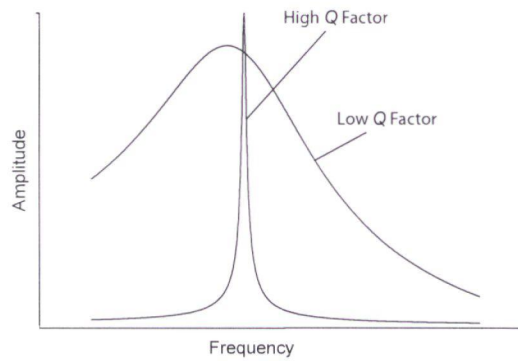


Figure 1.6: Decrease in the quality factor due to viscous damping produces a broader frequency response. The minimum value of Δf that can be detected is significantly reduced.

A method to control the Q factor using feedback was suggested a few years back [20], and it has been successfully used in atomic force microscope (AFM) cantilevers to increase their scanning speed in fluidic media [21] [22], because a higher Q implies a higher amount of energy is concentrated at the frequency of interest which implies slower scanning. It has also been used as a sensitive viscosity sensor [23] because Q and viscosity are related. The purpose of this thesis is to model a Q control method for precise mass measurement in fluidic environment. Q control will allow the detection of bioparticles to be performed in the native fluidic environment rather than in artificial environments like air or vacuum. With the problem of frequency shift resolution minimized, the sensitivity of the measurement method depends only on the size of the cantilever beam. With current cutting edge fabrication technologies (such as electron beam lithography), beams small enough to detect single biomolecules in their native fluidic environment can be fabricated [24].

1.4 Thesis Outline

Chapter 2 gives an analytical background on the different governing physical principles. The first section describes the vibrations of a cantilever beam. The governing PDE for the cantilever vibration is derived. Once the PDE is obtained, a technique for discretizing the PDE, known as *normal coordinate transformation*, is then described. This method is helpful in understanding the ROM extraction technique to be described later. A useful relationship for approximating the resonant frequency of a cantilever beam is then derived using energy methods. The following section discusses electrostatic actuation using the parallel plate capacitance. The relationships obtained give insights into the behavior of the structure, especially the pull-in phenomenon. Damping is a key parameter for this work and hence different reasons as to why damping arises are explored. Some analytical models for viscous damping are also described. The final section of Chapter 2 details a technique to reduce viscous damping using the velocity feedback technique.

Chapter 3 gives a detailed description of a popular numerical method known as the *finite element method* (FEM). This background is a prerequisite for intelligent use of FEM packages. A commercial FEM package, ANSYS, is used for this research because of its flexibility and support for multi-domain simulations. A brief overview of the ANSYS package is provided. The rest of the chapter gives a comprehensive account of the numerical simulations performed for the vibrating cantilever beam in a viscous environment and a comparison of the results with the analytical relationships provided in Chapter 2.

Chapter 4 discusses system level modeling and simulation of the cantilever sensor. The ROM technique mentioned previously is explained in detail. Then, the element in ANSYS that supports ROM extraction is described. This element allows for VHDL-AMS code export, which can be used in system level simulators. The ROM element is used within ANSYS to perform damped harmonic analysis. The results are compared to a full FEM simulation and are found to be very close despite the fact that the FEM simulation takes much longer to complete. The lumped parameters from the VHDL-AMS code were then used in a Simulink simulator to design a feedback control to reduce damping. The last section of chapter 4 discusses the importance of experimental verification and different measurement techniques for dynamic MEMS.

The final chapter concludes the thesis and provides some guidelines for potential future work.

Chapter 2

Analytical Background

This chapter provides the analytical framework for the modeling of the cantilever beam sensor. Most of the physical phenomena are governed by partial differential equations (PDE) and their associated boundary and initial conditions. Even though, for most cases, the PDEs have no closed form solutions, it is useful to understand their derivation and approximate analytical solutions as these provide insight on the phenomena. For more accurate results, numerical methods are required, as discussed in Chapter 3.

2.1 Cantilever Beam Vibration

This section first derives the governing PDE for cantilever vibrations. Once the PDE is obtained, a discretization technique using normal coordinate transformations is described. Finally, an approximation technique to determine the cantilever resonant frequency is developed.

2.1.1 Governing Partial Differential Equation

To formulate the continuum equation of motion for a cantilever beam, consider a uniform beam, shown in Figure 2.1 [25]. The beam has length L , width w , thickness T , mass m and flexural stiffness γI where γ is the Young's modulus and I is the moment of inertia. The general force p is applied and acts in the z direction, perpendicular to the axial axis of the beam. The derived equation is the same for different end-support boundary conditions. The cantilever beam is a special case with one end free and the other fixed.

The governing equation of motion of the beam can be derived by considering the equilibrium of forces and moments acting on a differential segment of the beam dx shown in Figure 2.1 and

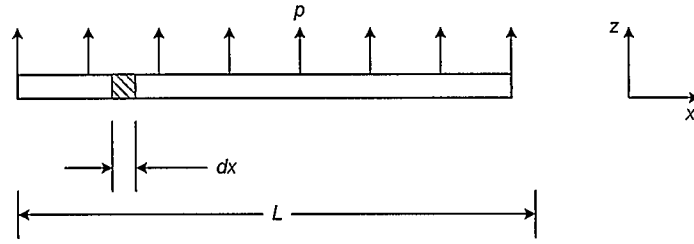


Figure 2.1: Uniform beam subjected to dynamic loading per unit length p .

magnified in Figure 2.2. Summing all the forces acting vertically as shown in Figure 2.2, we have

$$V + p dx - \left(V + \frac{\partial V}{\partial x} dx \right) - f_i dx = 0 \quad (2.1)$$

where V represents the internal shear force of the beam section and f_i is the transverse force per unit length.

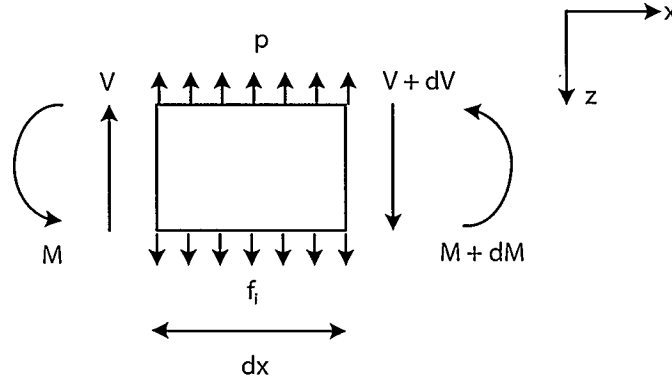


Figure 2.2: Forces and moments acting on a differential element dx .

But the inertial force is a product of the differential mass and the local acceleration

$$f_i dx = m dx \frac{\partial^2 z}{\partial t^2} \quad (2.2)$$

Substituting Equation 2.2 into Equation 2.1 and simplifying, we obtain

$$\frac{\partial V}{\partial x} = p - m \frac{\partial^2 z}{\partial t^2} \quad (2.3)$$

The moment equilibrium relationship is obtained by summing the moments about the elastic axis at the right edge giving

$$M + Vdx - \left(M + \frac{\partial M}{\partial x} dx \right) = 0 \quad (2.4)$$

This equation simplifies to

$$\frac{\partial M}{\partial x} = V \quad (2.5)$$

Note that the inertial forces do not contribute to the case of moment equilibrium. Differentiating Equation 2.5 with respect to x and substituting into Equation 2.3, we obtain

$$\frac{\partial^2 M}{\partial x^2} + m \frac{\partial^2 z}{\partial t^2} = p \quad (2.6)$$

For small angles of beam deflection, the moment is related to the second derivative of z (curvature) as [26]

$$M = \gamma I \frac{\partial^2 z}{\partial x^2} \quad (2.7)$$

Substituting Equation 2.7 into 2.6, we obtain a fourth order partial differential equation (PDE) in z governing the motion of a uniform beam

$$\frac{\partial^2}{\partial x^2} \left(\gamma I \frac{\partial^2 z}{\partial x^2} \right) + m \frac{\partial^2 z}{\partial t^2} = p \quad (2.8)$$

Equation 2.8 does not take into account the mechanisms which absorb energy from the structure during its dynamic response. The main mechanism of interest to this work is viscous damping, which to the first order is proportional to the velocity of the beam. If we represent the viscous force by f_D given by

$$f_D = c \frac{\partial z}{\partial t} \quad (2.9)$$

where the proportionality constant c is known as the damping factor, then we can rewrite Equation 2.3 with this extra force term

$$\frac{\partial V}{\partial x} = p - m \frac{\partial^2 z}{\partial t^2} - c \frac{\partial z}{\partial t} \quad (2.10)$$

Incorporating the damping term into the governing equation, we have

$$\frac{\partial^2}{\partial x^2} \left(\gamma I \frac{\partial^2 z}{\partial x^2} \right) + m \frac{\partial^2 z}{\partial t^2} + c \frac{\partial z}{\partial t} = p \quad (2.11)$$

Equation 2.11 cannot be easily analyzed in its continuous form. A discretization method which expresses the equation in different modes allows a more insightful analysis. This method will be described next.

2.1.2 Discretization Using Normal Coordinate Transformation

To be able to express the governing PDE into a discrete form, we need to introduce the concept of a normal coordinate transformation. The continuous displacement z in Equation 2.11 can be expressed as a sum of different modes where each mode z_n is given by

$$z_n = \Phi_n Y_n \quad (2.12)$$

where Φ_n is the n^{th} mode shape function and Y_n is the n^{th} modal amplitude. The mode shape functions are basis functions and serve the same purpose as the trigonometric functions in a Fourier series expansion with similar advantages — that is, they are orthogonal functions and also they describe the displacements efficiently so that only a few terms are required to provide a good approximation [25]. The total displacement z is obtained by summing up the modal components

$$z = \Phi_1 Y_1 + \Phi_2 Y_2 + \cdots + \Phi_N Y_N = \sum_{n=1}^N \Phi_n Y_n \quad (2.13)$$

In this equation, it can be seen that the shape function Φ_n serves to transform from the discrete coordinates Y_n to the continuous coordinates z . This is usually called *normal-coordinate* transformation [25].

Now, applying the transformation to the PDE of Equation 2.11, we obtain

$$\sum_{i=1}^{\infty} \frac{d^2}{dx^2} \left[\gamma I \frac{d^2 \Phi_i}{dx^2} \right] Y_i(t) + \sum_{i=1}^{\infty} m \Phi_i(x) \ddot{Y}_i(t) + \sum_{i=1}^{\infty} c \Phi_i(x) \dot{Y}_i(t) = p(x, t) \quad (2.14)$$

where the dot notation for the Y variable indicates a differentiation with respect to time. Multiplying by Φ_n and integrating with respect to x over the length L of the beam, we get

$$\begin{aligned} \sum_{i=1}^{\infty} Y_i(t) \int_0^L \Phi_n \frac{d^2}{dx^2} \left[\gamma I \frac{d^2 \Phi_i}{dx^2} \right] dx + \sum_{i=1}^{\infty} \dot{Y}_i(t) \int_0^L m \Phi_n \Phi_i(x) dx \\ + \sum_{i=1}^{\infty} \ddot{Y}_i(t) \int_0^L c \Phi_n \Phi_i(x) dx = \int_0^L \Phi_n p(x, t) dx \end{aligned} \quad (2.15)$$

Two orthogonality conditions related to mass and stiffness properties can be used to simplify this equation [25]. The orthogonality conditions are for two mode shape functions Φ_m and Φ_n where the frequencies of the two modes are different. The mass related orthogonality condition is

$$\int_0^L m \Phi_m \Phi_n dx = 0 \quad (2.16)$$

and the stiffness related orthogonality condition is

$$\int_0^L \Phi_m \frac{d^2}{dx^2} \left[\gamma I \frac{d^2 \Phi_n}{dx^2} \right] dx = 0 \quad (2.17)$$

Note that these conditions imply that for the two integrals in Equations 2.16 and 2.17, the only non-zero value occurs when the frequencies of the two mode shape functions are the same, i.e. when $\Phi_m = \Phi_n$. For viscous damping, c is proportional to the mass of the beam and we can write

$$c = a_0 m \quad (2.18)$$

and hence the mass orthogonality condition of Equation 2.16 applies. Applying the orthogonality conditions to Equation 2.15, the summations vanishes except when the mode shape functions have the same frequencies to obtain

$$\begin{aligned} \ddot{Y}_n(t) \int_0^L m \Phi_n^2(x) dx + \dot{Y}_n(t) a_0 \int_0^L m \Phi_n^2(x) dx \\ + Y_n(t) \int_0^L \Phi_n(x) \frac{d^2}{dx^2} \left[\gamma I \frac{d^2 \Phi_n}{dx^2} \right] dx = \int_0^L \Phi_n(x) p(x, t) dx \end{aligned} \quad (2.19)$$

It can be shown that [25]

$$\int_0^L \Phi_n(x) \frac{d^2}{dx^2} \left[\gamma I \frac{d^2 \Phi_n}{dx^2} \right] dx = \omega_n^2 \int_0^L m \Phi_n^2(x) dx \quad (2.20)$$

where ω_n is the natural frequency of the mode shape n . Therefore, Equation 2.19 can be written as

$$\begin{aligned} \ddot{Y}_n(t) \int_0^L m \Phi_n^2(x) dx + \dot{Y}_n(t) a_0 \int_0^L m \Phi_n^2(x) dx \\ + Y_n(t) \omega_n^2 \int_0^L m \Phi_n^2(x) dx = \int_0^L \Phi_n(x) p(x, t) dx \end{aligned} \quad (2.21)$$

The generalized mass, which is mass given in the generalized discrete coordinate system, is defined as

$$M_n = \int_0^L m \Phi_n^2(x) dx \quad (2.22)$$

Substituting Equation 2.22 into Equation 2.21, we get

$$\ddot{Y}_n(t) M_n + \dot{Y}_n(t) a_0 M_n + Y_n(t) \omega_n^2 M_n = P_n(t) \quad (2.23)$$

where

$$P_n(t) = \int_0^L \Phi_n(x)p(x,t)dx \quad (2.24)$$

is the load applied for mode n . Substituting back Equation 2.18 into Equation 2.23 and using the notation C_n for the damping coefficient related to mode n , we have

$$\ddot{Y}_n(t)M_n + \dot{Y}_n(t)C_n + Y_n(t)\omega_n^2M_n = P_n(t) \quad (2.25)$$

And finally introducing the modal stiffness K_n as

$$K_n = \omega_n^2M_n \quad (2.26)$$

we have the equation in a standard second order system as

$$\ddot{Y}_n(t)M_n + \dot{Y}_n(t)C_n + Y_n(t)K_n = P_n(t) \quad (2.27)$$

This equation is a discrete representation of Equation 2.11 with infinite number of modes. For the purpose of this work, we are interested in the first few modes. Equation 2.27 will be dealt with further when discussing the ROM technique in Chapter 4. However, for each mode, we have an equation of the form

$$m\ddot{z} + c\dot{z} + kz = F \quad (2.28)$$

where m , c and k are the effective mass, effective damping, and effective stiffness for that particular mode, respectively, and F is the force applied. It is very important to understand the characteristics of this equation to get insights on the workings of the mass sensor. The following section provides the solution to this equation and points out the important characteristics of its system response.

2.1.3 Single Degree of Freedom Equation

Equation 2.28 describes the vibration of the cantilever and the first step in solving the equation is to find the solution of the homogeneous equation, whereby the external force is zero. This gives

the natural response of the system. With no external force we have

$$m\ddot{z} + c\dot{z} + kz = 0 \quad (2.29)$$

The solution of Equation 2.29 has the form

$$z(t) = Ge^{st} \quad (2.30)$$

where G is a constant. Substituting back into Equation 2.29 leads to

$$(ms^2 + cs + k)Ge^{st} = 0 \quad (2.31)$$

If we introduce the resonant (sometimes referred to as natural) frequency ω_o as

$$\omega_o^2 = \frac{k}{m} \quad (2.32)$$

we have

$$s^2 + \frac{c}{m}s + \omega_o^2 = 0 \quad (2.33)$$

Equation 2.33 is a quadratic equation in the complex variable s and its solution is

$$s = -\frac{c}{2m} \pm \sqrt{\left(\frac{c}{2m}\right)^2 - \omega_o^2} \quad (2.34)$$

This expression represents three different types of motion depending on whether the value under the square root (the radical) is negative, zero, or positive. When the radical is zero, this is known as *critical damping* and the damping coefficient c_c for this particular case is given by

$$c_c = 2m\omega_o \quad (2.35)$$

In physical terms, c_c is the minimum damping coefficient where oscillations will not occur. Hence, for the purpose of this work, the critical damping case and the overdamped case (when

the radical is greater than c_c) are irrelevant. We are only interested in cases where vibrations will occur. This type of motion is called an *underdamped response*. To evaluate the underdamped natural response of the system, it is convenient to introduce the damping *ratio* ξ as the ratio of the damping coefficient to c_c

$$\xi = \frac{c}{2m\omega_o} \quad (2.36)$$

Then, we can write Equation 2.34 as

$$s = -\xi\omega_o \pm \sqrt{(\xi\omega_o)^2 - \omega_o^2} \quad (2.37)$$

Introducing damped vibration frequency ω_d as

$$\omega_d = \omega_o \sqrt{1 - \xi^2} \quad (2.38)$$

we have

$$s = -\xi\omega_o \pm j\omega_d \quad (2.39)$$

where $j = \sqrt{-1}$. Substituting Equation 2.39 to Equation 2.30, we get the displacement response of the form

$$z(t) = e^{-\xi\omega_o t} (G_1 e^{j\omega_d t} + G_2 e^{-j\omega_d t}) \quad (2.40)$$

This can be written as

$$z(t) = e^{-\xi\omega_o t} (A \sin(\omega_d t) + B \cos(\omega_d t)) \quad (2.41)$$

Applying initial conditions and solving for the coefficients A and B , we have

$$z(t) = e^{-\xi\omega_o t} \left(\frac{\dot{z}(0) + z(0)\xi\omega_o}{\omega_d} \sin(\omega_d t) + z(0) \cos(\omega_d t) \right) \quad (2.42)$$

Equation 2.42 can be written as

$$z(t) = z_o e^{-\xi \omega_o t} \cos(\omega_d t - \theta) \quad (2.43)$$

where

$$z_o = \sqrt{\left(\frac{\dot{z}(0) + z(0)\xi\omega_o}{\omega_d}\right)^2 + z(0)^2} \quad (2.44)$$

and

$$\theta = \arctan \frac{\dot{z}(0) + z(0)\xi\omega_o}{\omega_d z(0)} \quad (2.45)$$

Figure 2.3 shows a typical underdamped response. One method of estimating the value of ξ is by looking at the successive peak as shown with amplitudes z_1 and z_2 in Figure 2.3. The ratio of two successive peaks at z_n and z_{n+1} is given by

$$\frac{z_n}{z_{n+1}} = \exp\left(2\pi\xi\frac{\omega_o}{\omega_d}\right) \quad (2.46)$$

For low values of damping, i.e. $\omega_o \approx \omega_d$, ξ can then be approximated as

$$\xi \approx \frac{z_n - z_{n+1}}{2\pi z_{n+1}} \quad (2.47)$$

Response to Harmonic Loading

Of more relevance to this work, is the response of the cantilever beam to a harmonic loading. The unloaded solution obtained previously is the homogeneous part and, for the complete solution, we have to find the particular solution. When a harmonic external load is applied, Equation 2.28 can be written as

$$m\ddot{z} + c\dot{z} + kz = F_o \sin \omega t \quad (2.48)$$

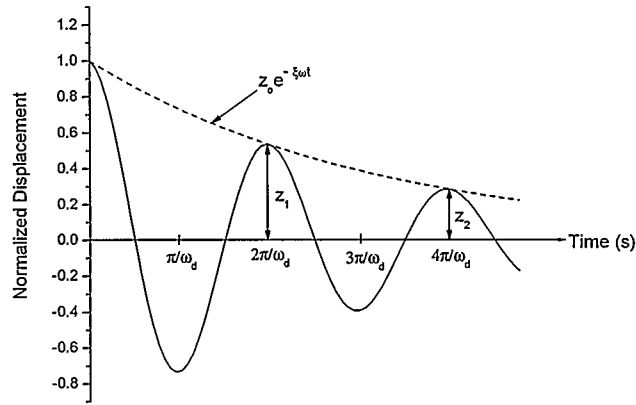


Figure 2.3: A typical underdamped response.

Dividing through by m and applying Equations 2.36 and 2.32, we can write

$$\ddot{z} + 2\xi\omega_o\dot{z} + \omega_o^2 z = \frac{F_o}{m} \sin \omega t \quad (2.49)$$

The complementary solution of this equation is the free vibration response given by Equation 2.41. Because of harmonic loading, the particular solution $z_p(t)$ has the form

$$z_p(t) = G_3 \sin(\omega t) + G_4 \cos(\omega t) \quad (2.50)$$

Note that we need both the cosine and sine terms because, in general, the response of a damped system is not in phase with the applied force. Substituting Equation 2.50 into Equation 2.49, we can evaluate the value of the coefficients G_3 and G_4 as

$$G_3 = \frac{F_o}{k} \frac{1 - \beta^2}{(1 - \beta^2)^2 + (2\xi\beta^2)^2} \quad (2.51)$$

and

$$G_4 = \frac{F_o}{k} \frac{-2\xi\beta}{(1 - \beta^2)^2 + (2\xi\beta^2)^2} \quad (2.52)$$

where $\beta = \omega/\omega_o$ is the ratio of the applied load frequency to the natural vibration frequency. Hence, combining the complementary and the particular solutions, we obtain the general solution

$$z(t) = e^{-\xi\omega_o t} (A \sin(\omega_d t) + B \cos(\omega_d t)) + \frac{F_0}{k} \frac{1}{(1 - \beta^2)^2 + (2\xi\beta^2)^2} [(1 - \beta^2) \sin(\omega t) - 2\xi\beta \cos(\omega t)] \quad (2.53)$$

The first term represents the transient response to the applied force. Because we are more interested in the steady state response, this term can be ignored. The second term is the steady state response and it is out of phase with the applied loading, but the two terms have the same frequency. The steady state term can be written as

$$z(t) = z_o \sin(\omega t - \theta) \quad (2.54)$$

where

$$z_o = \frac{F_0}{k} \sqrt{\frac{1}{(1 - \beta^2)^2 + (2\xi\beta^2)^2}} \quad (2.55)$$

and

$$\theta = \arctan \frac{2\xi\beta}{1 - \beta^2} \quad (2.56)$$

An important parameter for studying resonant response to be discussed later is the ratio of the resultant amplitude at a certain frequency to the static displacement known as the *dynamic magnification factor* D given by

$$D = \frac{z_o}{F_o/k} = \sqrt{\frac{1}{(1 - \beta^2)^2 + (2\xi\beta^2)^2}} \quad (2.57)$$

A plot of D as a function of frequency represents the frequency response of the displacement. The plot of D as a function of normalized frequency is shown in Figure 2.4 for different values of damping ratio ξ . The quality factor Q which was described in Chapter 1 is related to ξ as

$$Q = \frac{1}{2\xi} \quad (2.58)$$

Equation 2.58 implies that the higher the Q , the lower the damping ratio ξ . As can be seen in Figure 2.4, a higher Q implies a narrower response similar to what was described in Chapter 1, Figure 1.3. In Figure 2.4, note that the peak steady-state response occurs when $\beta = 1$ (i.e. when $\omega = \omega_o$). This phenomenon is known as *resonance*. At this frequency, the magnification factor D is given by

$$D_{\beta=1} = \frac{1}{2\xi} \quad (2.59)$$

However, for a general damped system, $\beta = 1$ is not the peak response. When Equation 2.57 is differentiated with respect to β and equated to zero, the peak D is found to depend on damping as

$$D_{max} = \frac{1}{2\xi\sqrt{1-\xi^2}} \quad (2.60)$$

For small values of ξ , it can be assumed that $D_{\beta=1} \approx D_{max}$, but in cases of viscous fluids, this approximation is not accurate.

From the preceding discussions, it can be seen that the resonant frequency of the cantilever beam has a significant influence on its dynamic characteristics. An approximate method for quick determination of ω_o as a function of geometry and material properties will be useful without resorting to numerical solutions. One of the most popular methods based on the principle of conservation of energy is Rayleigh's method [25], which will be discussed next.

2.1.4 Resonant Frequency Approximation — Rayleigh's Method

Rayleigh's method uses the fact that for an undamped system, the energy of the system has to be conserved; hence, the maximum potential energy must equal the maximum kinetic energy of the

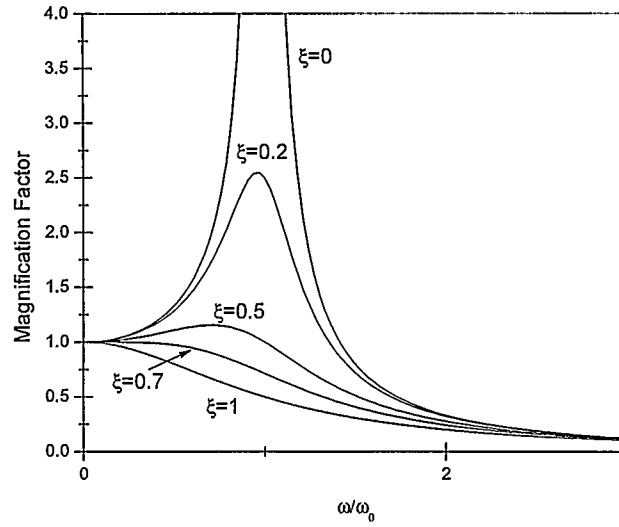


Figure 2.4: Variation of D with normalized frequency for different values of damping ratio.

system at resonance. For an oscillating cantilever, the potential energy is given by [25]

$$P.E = \frac{1}{2} \frac{3\gamma I}{L^3} z_o^2 \quad (2.61)$$

where z_o is the maximum beam displacement, and the kinetic energy is given by

$$K.E = \frac{33}{140} \frac{m}{2} \omega_o^2 z_o^2 \quad (2.62)$$

Equating the two energies, we get the resonant frequency as a function of geometry and material properties

$$\omega_o = 3.57 \sqrt{\frac{\gamma I}{m L^3}} \quad (2.63)$$

But the stiffness k of the cantilever is given by [26]

$$k = \frac{3\gamma I}{L^3} \quad (2.64)$$

Therefore, the resonant frequency can be written as

$$\omega_{o1} = \sqrt{\frac{k}{0.236m}} \quad (2.65)$$

with the 1 in the subscript emphasizing the fundamental (first) mode. By using the eigenmode expansion, which finds approximate effective spring constants for the different vibration modes [27], the resonant frequencies of the higher modes can be expressed as multiples of this fundamental mode. The second mode is given as [27]

$$\omega_{o2} = 6.267\omega_{o1} \quad (2.66)$$

where ω_{o1} is the fundamental resonant frequency. Rayleigh's method always overestimates the value of the resonant frequency because it depends on the selection of shape functions used to derive the kinetic and potential energy expressions. Any shape function that is different from the exact one will stiffen the system thus increasing the resonant frequency. However, it is an excellent method for first-order approximations. In the next chapter, the results obtained from finite element simulations will be compared to the Rayleigh approximation.

2.1.5 Resonant Frequency Shift for Mass Measurement

As seen in Equation 2.65, the resonant frequency is inversely proportional to the mass of the beam. If an extra mass is added on the beam, the resonant frequency changes as

$$\omega_{o1}^* = \sqrt{\frac{k}{0.236m + m_l}} \quad (2.67)$$

where m_l is the loaded mass and the star notation indicates the loaded resonant frequency. Rearranging Equations 2.65 and 2.67, we get

$$\frac{1}{\omega_{o1}^2} = \frac{0.236m}{k} \quad (2.68)$$

and

$$\frac{1}{\omega_{o1}^{*2}} = \frac{0.236m + \hat{m}_l}{k} \quad (2.69)$$

respectively. Rearranging and substituting frequency $\omega = 2\pi f$, we get the added mass m_l as

$$m_l = \frac{k}{4\pi^2} \left(\frac{1}{f_o^{*2}} - \frac{1}{f_o^2} \right) \quad (2.70)$$

By using similar arguments and Equation 2.66, for the second mode, the change in mass is given by

$$m_l = \frac{6.267^2 k}{4\pi^2} \left(\frac{1}{f_o^{*2}} - \frac{1}{f_o^2} \right) \quad (2.71)$$

Hence, by measuring the shift in frequency, we can determine the value of the mass added on the beam. In Chapter 3, it will be shown that the second mode is less dependent on the positioning of the mass on the cantilever beam and it may yield better measurement results.

2.2 Electrostatic Actuation

Electrostatic actuation is the most common method used in MEMS devices because of its excellent scaling properties and ease of integration with CMOS electronics. The cantilever beam suspended on top of a polysilicon ground plane can be modelled as a parallel plate capacitor as shown in Figure 2.5, ignoring fringing effects since the area of the dimensions of the capacitor are much bigger than the gap between the beam and the ground plane [26].

For voltage-controlled actuation, the basic parameter is the charge generated by a voltage source as shown in Figure 2.6. If one plate is moveable and one is fixed, as we have for the case of the cantilever beam, then there are two ways to change the energy. The first one is by changing the charge on the plates, which is accomplished by changing the voltage between the plates. The second way is achieved mechanically by changing the gap between the plates.

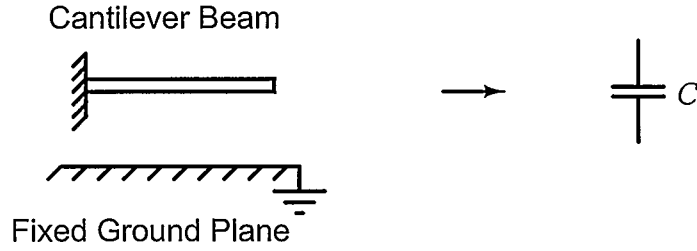


Figure 2.5: A conducting cantilever beam suspended on top of the ground plane is electrically equivalent to a capacitor C .

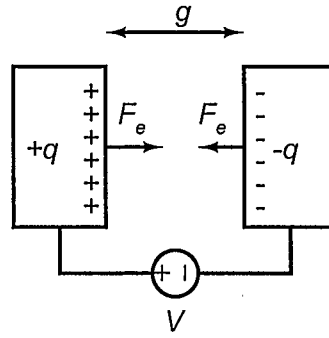


Figure 2.6: Electrostatic force F_e is from the opposite charges $+q$ and $-q$ built on the plates by the voltage source V .

Quantitatively, the change in energy dW can be expressed as

$$dW(q, g) = Vdq + F_e dg \quad (2.72)$$

where q is the charge on each surface (beam and ground plane), and g is the gap between the beam and the ground plane. To obtain the force as a function of the voltage, we need to introduce an abstract term of co-energy W^* defined as [26]

$$W^*(V, g) = qV - W(q, g) \quad (2.73)$$

where $W(q, g)$ is the energy expressed in Equation 2.72. Differentially, this becomes

$$dW^*(V, g) = (q dV + V dq) - dW(q, g) \quad (2.74)$$

Substituting Equation 2.72 into Equation 2.74, we have

$$dW^*(V, g) = q dV - F_e dg \quad (2.75)$$

From this expression, we obtain the equations for q and F_e as a function of co-energy

$$q = \left. \frac{\partial W^*(V, g)}{\partial V} \right|_{g=\text{constant}} \quad (2.76)$$

and

$$F_e = - \left. \frac{\partial W^*(V, g)}{\partial g} \right|_{V=\text{constant}} \quad (2.77)$$

For a fixed gap capacitor (no mechanical energy variation), while the voltage is varied, the co-energy is given by the integral

$$W^*(V, g) = \int_0^V q dV = \int_0^V CV dV = \int_0^V \frac{\epsilon A}{g} V dV \quad (2.78)$$

where A is the area of the plates. Integrating, we get the expression for co-energy W^*

$$W^*(V, g) = \frac{\epsilon AV^2}{2g} \quad (2.79)$$

Applying the differential expression of Equation 2.77, we get the expression for the electrostatic force F_e

$$F_e = \frac{\epsilon AV^2}{2g^2} \quad (2.80)$$

Now, if the gap is changing so that the original gap is given by g_0 and the displacement of the moving plate is given by z , then we have

$$g = g_0 - z \quad (2.81)$$

and the electrostatic force can be written as a function of the displacement z

$$F_e = \frac{\epsilon AV^2}{2(g_0 - z)^2} \quad (2.82)$$

Note that now the voltage determines the force, which increases z and feeding back to increase the force. This positive feedback results in instability that causes a phenomenon called “pull-in” where the moving plate snaps into the fixed plate. The following section derives the expression for the gap distance where this phenomenon occurs. Of more relevance to this work is pull-in at resonance, which has a different stability criterion from the static pull-in [28].

2.2.1 Pull-In Phenomena

To explore the stability of the equilibrium of the plate motion, consider the forces acting on the moving plate. The electrostatic force F_e is pulling the plate down while the elastic force is opposing the motion. The elastic force is given by the standard Hooke’s law

$$F = kz = k(g_0 - g) \quad (2.83)$$

Consequently, the total force acting on the moving plate is

$$F_T = k(g_0 - g) - \frac{\epsilon AV^2}{2g^2} \quad (2.84)$$

The equilibrium condition is $F_T = 0$. To see the effect of small perturbation of the gap δg on the force F_T , we can write [26]

$$\delta F_T = \left. \frac{\partial F_T}{\partial g} \right|_V \delta g \quad (2.85)$$

If δF_T is positive for positive δg , then that value of g is an unstable equilibrium point because a small increase in g creates a force that tends to increase it further (positive feedback). Hence, for stable equilibrium, we need a value of g that will give a negative δF_T . Evaluating δF_T , we have

$$\delta F_T = \left(\frac{\epsilon A V^2}{g^3} - k \right) \quad (2.86)$$

For stable equilibrium, this expression has to be negative, giving

$$k > \frac{\epsilon A V^2}{g^3} \quad (2.87)$$

At pull-in, the following equations have to be satisfied

$$k = \frac{\epsilon A V_{pi}^2}{g_{pi}^3} \quad (2.88)$$

and

$$F_T = 0 \quad (2.89)$$

where the subscript pi indicates value at pull-in. Equating Equations 2.84 and 2.88, we obtain

$$\frac{\epsilon A V_{pi}^2}{2g_{pi}^2(g_0 - g_{pi})} = \frac{\epsilon A V_{pi}^2}{g_{pi}^3} \quad (2.90)$$

Solving for g_{pi} , we obtain the point where pull-in occurs

$$g_{pi} = \frac{2}{3}g_0 \quad (2.91)$$

This means that for *static* stability, the plate can move only one third of the gap. Conversely, at resonance, it can be shown that the plate can move up to 0.56 times the gap without having stability problems [28]. The derivation for resonant pull-in is much more involved, and the reader is referred to Seeger et. al. [28]. This extra gap allows more room for actuation especially for small-gap electrostatic actuators like those implemented in the standard MUMPs process.

2.3 Damping

For conventional macro scale dynamic systems, the damping effects caused by the surrounding fluid can in general be ignored as they are not very significant. This is because fluid damping (also called *viscous* damping since it is caused by the viscosity of the fluid) is related to the surface area of the moving parts. The surface-to-volume ratio of macro scale systems is very small and thus the damping effects are insignificant. For MEMS, however, the surface-to-volume ratio is much larger and damping effects have a significant effect on their dynamics. Therefore, understanding the sources of damping and being able to quantify their effects is very crucial for proper dynamic MEMS design [29].

Damping is essentially an energy loss mechanism and it has a variety of sources. The damping can be classified as structural damping, caused by internal friction within the structures, contact damping which usually occurs at the points of contact between different structures and fluidic or viscous damping mentioned above because of the external media. Of the three sources, fluidic damping is very dominant and the only time when the other sources have to be considered is when the device is operated in vacuum, where there is negligible fluid damping. Accordingly, for the purpose of this research, all other sources are ignored and only fluid damping is considered.

When it comes to fluid damping, there are two main regimes to be considered depending on the gap g between the oscillating structure and a wall (usually the substrate or ground electrode) as shown in Figure 2.7.

When g is large, the fluid flows freely up and down tracking the beam. This regime is known as *drag* because the dissipation comes from the fluid applying drag force to the moving structure. However, when g is small, the fluid will be squeezed between the oscillating beam and the fixed wall. This phenomenon is called *squeeze film damping*, and it is very common for electrostatically actuated MEMS devices because the gaps are usually made small to maximize the electrostatic

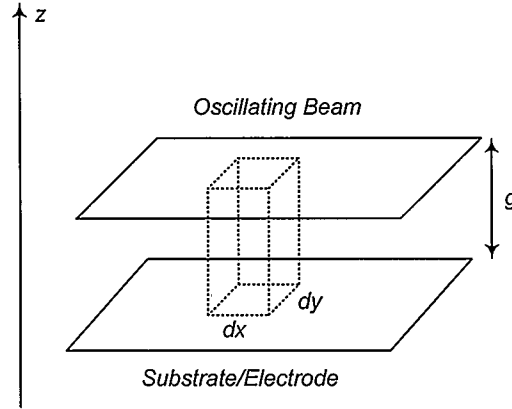


Figure 2.7: A column of fluid between two plates.

force. To obtain accurate behavior of fluid damping, the PDE governing fluid dynamics has to be solved. This PDE, known as the Navier-Stokes equation [26], is very complicated and numerical solutions are required to solve it. Chapter 4 will briefly touch up on the equation in the context of a numerical solution. Since we are interested in electrostatically actuated cantilever beam, the gap between the beam and the substrate is very small (on the order of few microns). Hence, drag force is not of interest and we will focus on the squeeze film phenomenon. The following subsections introduces approximate models for the squeeze film damping which will form the basis for the numerical solution in Chapter 4.

2.3.1 Squeeze Film Damping

Since it is very difficult to solve the Navier-Stokes equation, an approximation based on assumptions valid for most MEMS devices is usually used to calculate the squeeze film damping. Considering the Navier-Stokes equation with the following assumptions [26]

- The gap g_0 is much smaller than the lateral dimensions of the beam. This is usually the case, since the gap is made very small for electrostatic actuation to maximize the electrostatic force for a given voltage.

- The fluid viscous effects are much larger relative to the fluid inertial effects (quantitatively, this implies that the Reynold's number $Re \ll 1$).
- The system is isothermal. That is, any heat generated by dissipative effects is quickly absorbed by the walls. This is a good assumption due to the large surface to volume ratio of the MEMS devices.

we can obtain a simplified PDE known as the Reynold's equation. Reynold's PDE relates the pressure gradients to the fluid velocity and is given as

$$\frac{\partial}{\partial x} \left(\rho \frac{g^3}{\delta} \frac{\partial P}{\partial x} \right) + \frac{\partial}{\partial y} \left(\rho \frac{g^3}{\delta} \frac{\partial P}{\partial y} \right) = 12 \frac{d(g\rho)}{dt} \quad (2.92)$$

where ρ is the density of the fluid and δ is the viscosity of the fluid. The numerical solution of this equation can be obtained in ANSYS by using the FLUID136 element. However, to gain some insights on the squeeze film damping as it relates to the geometry and material properties of the structure, we can simplify Reynold's equation by assuming that g is uniform in both x and y directions, we obtain:

$$\frac{\partial^2 P}{\partial x^2} + \frac{\partial^2 P}{\partial y^2} = \frac{12\delta}{g^3} \frac{dg}{dt} \quad (2.93)$$

To obtain the squeeze film damping force for beam, consider the rectangular plate shown in Figure 2.8. If the beam is much longer compared to its width, the problem can be considered to be one-dimensional (pressure is only varying in the x direction).

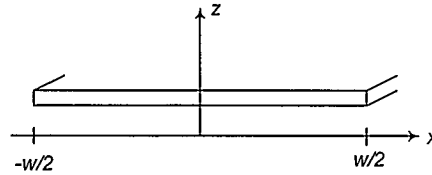


Figure 2.8: Top view of a chain of plates representing a cantilever beam.

Reynold's equation can then be written as [29]

$$\frac{d^2 P}{dx^2} = \frac{12\delta}{g^3} \frac{dg}{dt} \quad (2.94)$$

Integrating this equation twice and applying the boundary conditions, we obtain the pressure as a function of x

$$P(x) = -\frac{6\delta}{g^3} \left(\frac{w^2}{4} - x^2 \right) \frac{dg}{dt} \quad (2.95)$$

The negative sign indicates that the pressure is positive when the fluid film is squeezed (i.e. $dg/dt < 0$). The damping force on the plate is obtained by integrating the pressure over the area of the plate

$$F_{sf} = \int_{-w/2}^{w/2} P(x) L dx = -\frac{\delta w^3 l}{g_o^3} \dot{g} \quad (2.96)$$

Comparing this result with the second order dynamic equation described earlier, the coefficient of the velocity is the damping coefficient; therefore, we have

$$c_{sf} = \frac{\delta w^3 l}{g_o^3} \quad (2.97)$$

Substituting the value of damping ratio given by Equation 2.36, we have damping as a function of radial frequency ω_n as

$$\xi_{sfn} = \frac{c_{sf}}{2\rho w t l \omega_n} = \frac{\delta w^2}{2\rho t \omega_n g_o^3} \quad (2.98)$$

where n is the n th vibration mode. The quality factor is then obtained as

$$Q_{sfn} = \frac{\rho t g_o^3 \omega_n}{\delta w^2} \quad (2.99)$$

The values obtained here will be compared to the numerical results obtained from ANSYS in Chapter 3. The following subsection describes the effect of damping on measurement sensitivity.

2.3.2 Damping effect on measurement sensitivity

Chapter 1 showed qualitatively how a decrease in Q factor decreases measurement sensitivity for frequency modulation sensors. Now this issue will be discussed in a quantitative manner. To obtain an expression for the minimum *change* in mass ∂M_{min} that can be measured by the frequency modulation technique, a second order system approximation is used. A simple estimate of the change in mass required to shift the resonant frequency by its halfwidth i.e. $\omega_o \rightarrow (\omega_o + \partial\omega_o)$ is obtained by multiplying the change in resonant frequency by the inverse of what is called the frequency responsivity to added mass \Re [30] given by

$$\Re = \frac{\partial\omega_o}{\partial m} \quad (2.100)$$

Therefore we have the minimum change in mass as

$$\partial M_{min} \sim \frac{1}{\Re} \partial\omega_o = \left(\frac{\partial\omega_o}{\partial m} \right)^{-1} \partial\omega_o \quad (2.101)$$

But

$$\partial\omega_o \sim \frac{\omega_o}{2Q} \quad (2.102)$$

Hence

$$\partial M_{min} \sim \frac{2m}{\omega_o} \frac{\omega_o}{2Q} = \frac{m}{Q} \quad (2.103)$$

Therefore, it can be seen that the minimum detectable mass increases as the original mass of the beam decreases (smaller structures have more sensitivity) and the quality factor Q increases.

2.3.3 Practical Damping Factor Measurement

Section 2.1.3 discussed one method of determining ξ given by Equation 2.47. However, in practical situations, it is very difficult to obtain the time domain transient characteristics that will allow us

to measure the different peak values. This section explores two methods based on the frequency response of the cantilever beam displacement.

Resonant Amplification Method

The first frequency based method is based on the observation of steady state harmonic response behavior [25]. If harmonic forces with different frequencies are applied to the beam, we can obtain a frequency response plot as shown in Figure 2.9. From Equations 2.60 and 2.38 and noting that $D_{max} = z_{max}/z_{static}$, we have

$$\xi = \frac{1}{2} \frac{z_{static} \omega_o}{z_{max} \omega_d} \approx \frac{1}{2} \frac{z_{static}}{z_{max}} \quad (2.104)$$

with the last approximation applying for low damping coefficients. Note that this method relies on being able to obtain static displacement z_{static} which may not be possible in some cases.

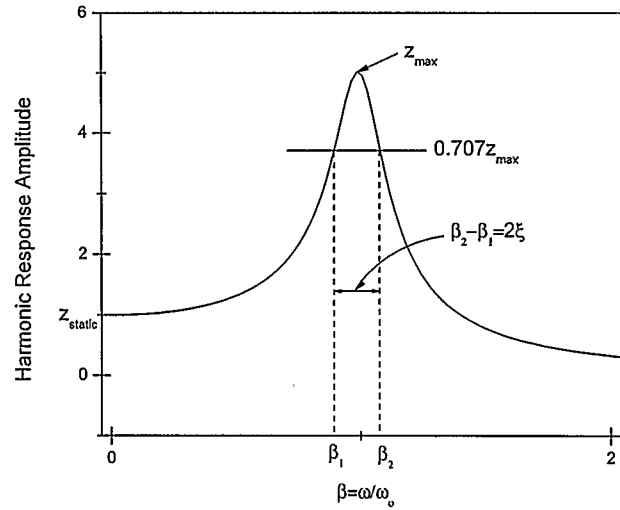


Figure 2.9: Frequency response curve obtained by sweeping the input force at different frequencies.

Half Power Bandwidth Method

Note that from Equation 2.55, the shape of the frequency response amplitude depends on the damping factor ξ . Therefore, by using the frequency response parameters, we can determine ξ . One of the most common parameters used is the half power bandwidth, defined as the amplitude where the power is half of the maximum power. This is related to z_{static} and Equation 2.55 as

$$\frac{1}{2\xi\sqrt{2}} = \sqrt{\frac{1}{(1 - \beta^2)^2 + (2\xi\beta^2)^2}} \quad (2.105)$$

Squaring both sides and solving for β^2 , we get

$$\beta^2 = 1 - 2\xi^2 \pm 2\xi\sqrt{1 + \xi^2} \quad (2.106)$$

Neglecting the ξ^2 term under the square root, we obtain the β values of

$$\beta_1 \approx 1 - \xi - \xi^2 \quad (2.107)$$

and

$$\beta_2 \approx 1 + \xi - \xi^2 \quad (2.108)$$

Combining these two expressions, we obtain ξ as a function of the two β values

$$\xi \approx \frac{1}{2}(\beta_2 - \beta_1) \quad (2.109)$$

This technique is illustrated graphically in Figure 2.9. Practically, both methods described in this section should be performed independently and the results compared to verify the accuracy of ξ .

2.4 Quality Factor Control

2.4.1 Q -Control Basics

As described in the previous section, each vibration mode of a cantilever beam can be modelled as a harmonic oscillator represented by Equation 2.28. If the beam is driven by a force F_1 given by

$$F_1 = F_0 e^{j\omega t} \quad (2.110)$$

and the motion of the cantilever is a sinusoid lagging behind the driving force by an angle ϕ

$$z = A e^{j(\omega t - \phi)} \quad (2.111)$$

then, if we have a positive feedback loop, that detects z , apply gain G and phase shift of $\pi/2$ to the signal and adds the resulting force F_2 to the original driving force, then we can write Equation 2.28 as

$$m\ddot{z} + c\dot{z} + kz = F_1 + F_2 = F_0 e^{j\omega t} + G e^{j\pi/2} z \quad (2.112)$$

But from Equation 2.111, we have the velocity of the cantilever as

$$\dot{z} = j\omega A e^{j(\omega t - \phi)} = \omega A e^{j(\omega t - \phi + \pi/2)} \quad (2.113)$$

with the second equality because

$$j = e^{j\pi/2} \quad (2.114)$$

From Equation 2.113, we have the velocity of the cantilever related to its displacement as

$$\dot{z} = \omega e^{j\pi/2} z \quad (2.115)$$

Substituting Equation 2.115 into Equation 2.112, we get

$$m\ddot{z} + c\dot{z} + kz = F_0 e^{j\omega t} + \frac{G}{\omega} \dot{z} \quad (2.116)$$

Rearranging, we obtain

$$m\ddot{z} + c^* \dot{z} + kz = F_0 e^{j\omega t} \quad (2.117)$$

where c^* is the effective damping factor given by

$$c^* = c - \frac{G}{\omega} \quad (2.118)$$

From Equation 2.118, it can be seen that the effective damping factor can be controlled by modifying the value of the feedback gain G . Figure 2.10 shows a block diagram for the setup required to achieve Q control.

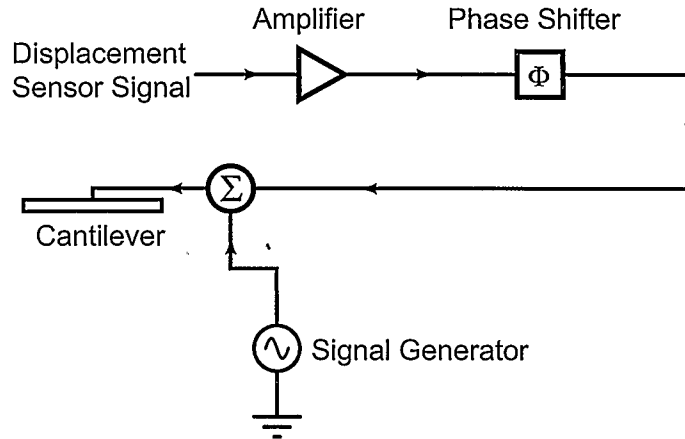


Figure 2.10: Setup used for Q control implementation expressed by Equation 2.112.

Chapter 3

Finite Element Modeling

This chapter describes a numerical method for solving PDEs known as the finite element method (FEM) and the commercial package used ANSYS. FEM is a vast field with varying backgrounds and it is changing rapidly with advances in computing and solution techniques. The background provided here is only so that the user of commercial FEM packages can use them intelligently and it is not supposed to be a comprehensive description. For further information the interested reader is referred to references [31], [32], [33]. For ANSYS specific techniques, a good starting point is [34].

First, an introductory overview of the FEM technique is provided. Then, the commercial FEM package ANSYS and its capabilities is described. Finally, the simulations performed in ANSYS for electrostatic actuation, cantilever vibration frequency, mass placement dependence on vibration modes and viscous damping are discussed. The FEM results are also compared to the analytical relationship described in the previous chapter for verification.

3.1 The Finite Element Method (FEM)

As discussed in the previous chapter, most physical phenomena are governed by partial differential equations. Generally, these equations with their corresponding boundary/initial conditions are very complex and can not be solved to yield closed formed analytical solution. Approximation methods based on subdividing (discretizing) the system into smaller and easier to solve components are usually employed. These methods, collectively known as numerical methods, come in a variety of flavors and their applicability depends on the nature of the problem to be discretized. Some of the more common numerical techniques for solving PDEs include finite difference method (FDM), finite element method (FEM) and boundary element method (BEM) [35]. FEM was originally

applied to structural analysis [32][31][34], but due to its general applicability, it has evolved and currently it is used in many different domains including fluid mechanics, electromagnetism and heat transfer.

The first and most crucial step in any numerical method is the *discretization* procedure, where a continuous body or field is divided into multiple smaller but easier to solve elements. This concept is illustrated in Figure 3.1. The elements are made up of nodes and different elements have different number of nodes. Usually, the elements with more number of nodes are more accurate even though they are more computationally expensive to solve [31]. This discretization procedure is known as meshing and proper meshing is a very important prerequisite for a good finite element simulation.

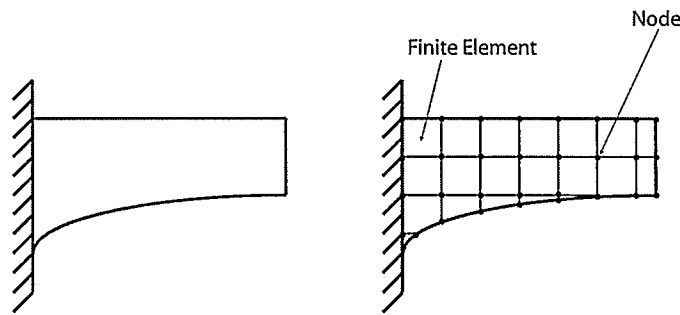


Figure 3.1: A plane structure of arbitrary shape shown on the left is discretized into simple finite elements shown on the right.

Once the system is discretized, boundary and initial conditions are applied and then the system can be solved. Several procedure exist on how to solve for the unknown parameters. There are three main types of solution methods known as the direct method, the variational method and the weighted residual method.

3.1.1 Direct Method

The direct method is the most intuitive of the three methods but it is limited to very simple problems where the form of the solution can be assumed. In structural problems, the assumed form is a

system of equations representing Hooke's law

$$[K]\{q\} = \{F\} \quad (3.1)$$

where $[K]$ is the stiffness matrix, $\{q\}$ is the nodal displacement vector which is the unknown and $\{F\}$ is the vector of applied nodal forces. Once the problem is setup in the matrix form, the unknown can be solved using standard matrix inversion techniques. In other domains, equivalent expressions can be obtained, for example in an electrical network, we have Ohm's law in matrix form

$$[R]\{i\} = \{v\} \quad (3.2)$$

where $[R]$ is the impedance matrix, $\{i\}$ is the nodal current vector (total current flowing into or out of the nodes) which is the unknown and $\{v\}$ is the vector of applied nodal potential differences. Even though the direct method is simpler to understand and implement, it is not flexible in terms of the problems it can be applied to and hence it is not used in commercial FEM software.

Variational and weighted residual methods are more general and they are based on approximating the exact solution with an approximate solution which is a linear combination of specific trial functions, typically polynomials [35]. If \bar{y} is the variable of interest, then it can be approximated as y , which is a linear combination of trial functions y_i

$$\bar{y} \approx y = \sum_{i=1}^N C_i y_i \quad (3.3)$$

The trial functions have to be selected such that they are independent of each other and the task that remains is to solve for the coefficients C_i such that y is a good approximation to the solution of the PDE. The variational and the weighted residual methods are used for this purpose.

3.1.2 The Variational Method

This method is based on a branch of mathematics known as variational calculus [35] whose object is to minimize a special type of function known as a functional, which is a function of a function. The simplest problem of the calculus of variations is minimization of the integral

$$F[\bar{y}(x)] = \int_a^b G(x, \bar{y}, \bar{y}') dx \quad (3.4)$$

where F is the functional, x is the independent variable and \bar{y} is the unknown. To minimize this functional, the condition that must be satisfied is what is known as the Euler equation

$$\frac{\partial G}{\partial y} - \frac{d}{dx} \left(\frac{\partial G}{\partial y'} \right) = 0 \quad (3.5)$$

To solve an FEM problem using the minimization approach, we need to find a functional F that yields the differential equation when it is minimized. In practice, this occurs in problems expressed in the form of energy and energy minimization yields the solution. Once the functional form is found, the approximate solution of Equation 3.3 is substituted into the functional and the functional is minimized to solve for the coefficients C_i .

3.1.3 The Weighted Residual Method

The weighted residual method is a member of a family of methods generally known as residual methods, in which the approximate form of the solution y is assumed and the residual R is defined by substituting the approximate solution into the exact differential equation [35]. The approximate solution is chosen in a similar manner as for the variational method, but the coefficients C_i are chosen so as to minimize R . There are two different methods used to minimize R : collocation method and the Galerkin method.

The Collocation Method

For the collocation method, once the trial functions are determined and expressed as Equation 3.3, the approximate solution y is substituted into the original differential equation. R is determined as

the error in the differential equation and it is a function of the coefficients C_i . When R is equated to zero, the corresponding C_i s are the one which minimizes the residual (error).

The Galerkin Method

For the Galerkin method, instead of minimizing the residual directly, the residual is weighted by multiplying by some weighting functions W_j , integrating the weighted residuals over the range of interest, and setting the integrals to zero to give equations for the evaluation of coefficients C_i . This method is found to give exceptionally good results in practice and it is used in most commercial packages [35].

To sum up, there are a variety of ways of solving an FEM problem, but in most practical cases, either the Galerkin weighted residual method or the variational method is used depending on the nature of the problem. In some domains, especially in solid mechanics, the problems are usually set up using energy principles and it is natural to use a variational approach to solve them. On the other hand, most problems in heat transfer, fluid mechanics and electromagnetism, the governing PDEs are known and in this case, it is more convenient to use the Galerkin weighted residual approach. Figure 3.2 tabulates the different techniques with their advantages and disadvantages.

Finite Element Method	Advantages	Disadvantages
Direct Method	<ul style="list-style-type: none"> ○ Intuitive and easy to understand. ○ Very easy to implement on the computer. 	<ul style="list-style-type: none"> ○ Only applicable to very trivial problem since it becomes very cumbersome for complex problems.
Variational Method	<ul style="list-style-type: none"> ○ Based on energy minimization formulation resulting in tremendous flexibility. 	<ul style="list-style-type: none"> ○ Difficult to program.
Weighted Residual Method	<ul style="list-style-type: none"> ○ Based on energy minimization formulation resulting in tremendous flexibility. 	<ul style="list-style-type: none"> ○ Difficult to program.

Figure 3.2: A summary of different FEM techniques with their advantages and disadvantages.

3.2 The ANSYS FEM Software

ANSYS is a comprehensive FEM package originally released in 1971 [34]. Currently, the latest ANSYS release is 8.1 which comes with different modules including structural, thermal, fluidic, electromagnetic and acoustic. ANSYS also allows what is known as Multiphysics simulations where the different domains are coupled. This is very important for MEMS transducers design since by definition, for a transducer, more than one energy domain is involved and they are usually coupled.

A typical FEM analysis in ANSYS involves three main steps — preprocessing, solution and postprocessing. In the preprocessing step, known as the PREP7 processor in ANSYS, the user defines the model, material properties, elements to be used and performs the meshing. If modeling in ANSYS is cumbersome, the solid models can be designed in other design software and imported into ANSYS in a standard IGES format. The user has to be careful with meshing the imported models since sometimes the models may need slight modifications before they can be properly meshed.

Once the preprocessing phase is done, ANSYS enters into the solution phase. In this phase, the user specifies what kind of analysis should be done. The most common types of analyses are static, harmonic, modal and transient. Then, the user specifies boundary conditions. These are necessary to avoid indeterminate problems (where there are more unknowns than the number of equations). ANSYS then solves for the unknowns in the PDEs or the energy formulation.

The final phase is the postprocessing phase. Postprocessing allows the user to display the results in a user-friendly manner and also calculate other parameters of interest based on the basic unknowns solved by ANSYS. Two postprocessors are available in ANSYS. The first one, known as the POST1 is used to plot and analyze time-independent parameters. POST26, is the time-history postprocessor and is used for transient analyses where the variation of parameters with time is

important.

3.3 Electrostatic Actuation

The beam displacement due to the electrostatic force was obtained by performing a coupled domain electrostatic-structural simulation. When performing coupled domain simulation, it is important to make sure that the elements between the different regions are compatible with each other. In the case of three dimensional electrostatic-structural coupling, SOLID45 element in the structural domain and SOLID123 element in the electrical domain are compatible. The meshing strategy used in all the ANSYS simulations was to start with a very coarse simulation just to make sure that the results roughly make sense. Then, the mesh density was doubled until the results were not changing up to 3 decimal places. This is a good strategy to determine the appropriate mesh density for a given problem [31]. Figure 3.3 shows the mesh for the two domains. The top volume is the SOLID45 brick mesh while the bottom volume is the SOLID123 tetrahedral mesh representing the gap between the cantilever beam and the substrate.

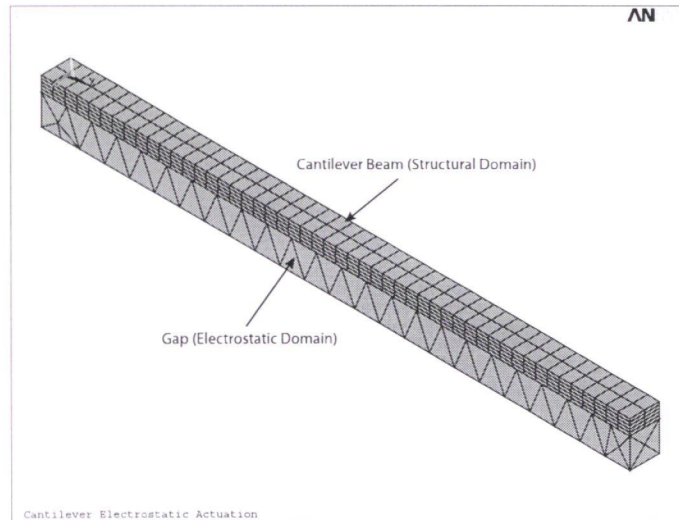


Figure 3.3: SOLID45 brick elements represent the structural domain while SOLID123 tetrahedral element represent the electrostatic domain.

To verify the applicability of Equation 2.80 for different values of the voltage, a parametric analysis was done with varying voltage from 10V to 100V. The boundary conditions for the electrostatic domain were applied with 0V at the bottom boundary and the sweeping voltage at the top boundary. Morphing option was enabled to allow for the fact that as the structure deforms, the gap region also changes. The morphing option allows for mesh deformation. Figure 3.4 shows the beam deformation for the case when 100V was applied on the cantilever beam. The displacement at the tip of the beam is $0.314 \mu\text{m}$. Figure 3.5 shows the comparison between the ANSYS coupled simulation and the electrostatic force approximation obtained by Equation 2.80. The analytical approximation value for beam displacement was obtained by taking the value of force from Equation 2.80 and applying Hooke's law as

$$F = kx \quad (3.6)$$

where k is the stiffness of the beam and x is the beam displacement. It is easy to see that this approximation overestimates the displacement since in reality the electrostatic force is distributed throughout the beam but for this calculation, we are assuming that the total force is concentrated at the end of the beam. This explains the approximate results being larger than the ANSYS results even though they have similar trends. Figure 3.6 is a plot of the beam displacement as a function of the square of the applied voltage. As expected, the curves follow a linear characteristic.

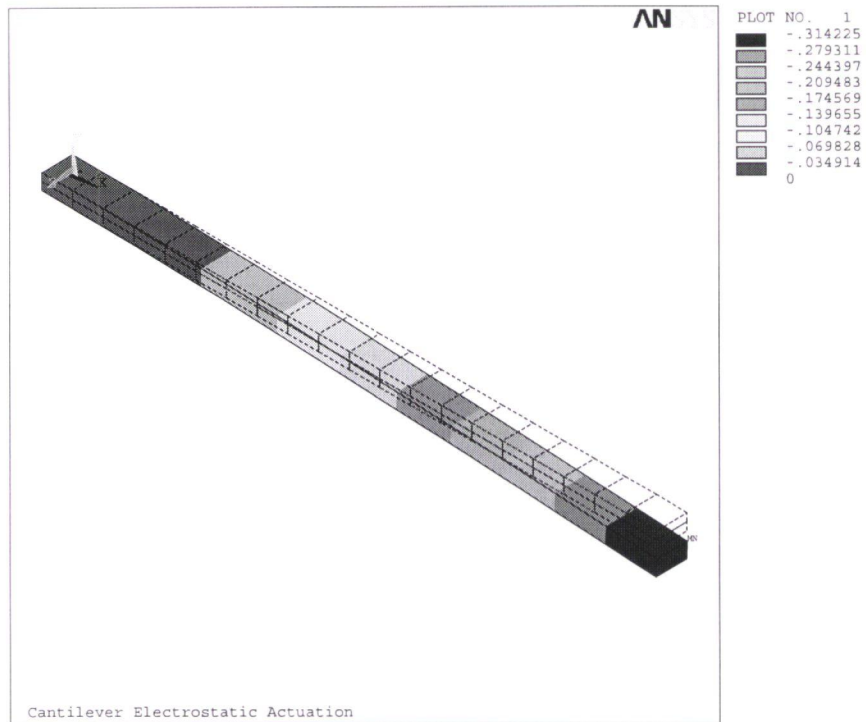


Figure 3.4: Beam deformation when 100V is applied to the cantilever beam with respect to the ground plane.

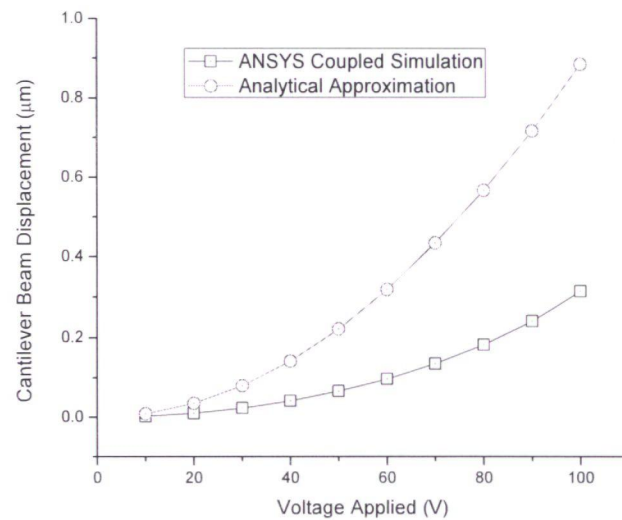


Figure 3.5: The comparison between the analytical and FEM results for the beam displacement as a function of the voltage.

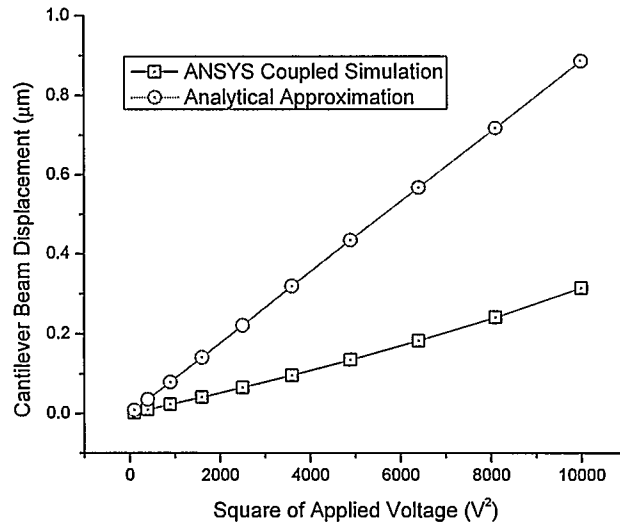


Figure 3.6: The comparison between the analytical and FEM results for the beam displacement as a function of the square of the applied voltage. The curves shows a linear relationship as expected.

3.4 Cantilever Vibration Frequency

ANSYS supports different kinds of structural dynamic analysis including static, modal, harmonic and transient analysis. The modal analysis is used to calculate the mode shapes of vibration. These modes are similar to the mode shape functions described in the previous chapter. Once the mode shapes are determined, harmonic analysis is then used to find the resonant frequencies associated with the different modes. An excellent description of how the modal and harmonic analysis are related can be found in [2]. Figure 3.7 illustrates this relationship for a tuning fork. It can be seen that the harmonic response tells us about the amplitude of a given point on the structure as a function of frequency while modal response provide information about the amplitude of different points (spatial distribution) of the structure at the same frequency. Hence, to get a complete dynamic response of the structure, both analysis have to be performed.

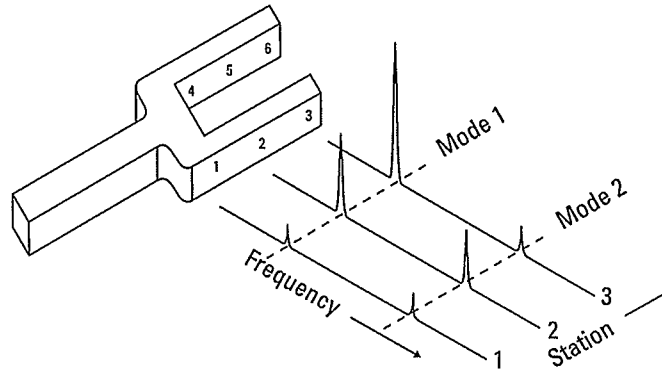


Figure 3.7: The relationship between the modal response and the harmonic response for a tuning fork. Adapted from [2].

The ANSYS elements used for modal analysis were the 3-D structural elements. Two elements with differing accuracy were used. SOLID45 is an 8-node 3-D element (x , y and z degrees of freedom) and SOLID95 is a 20-node 3-D element. For each beam, the simulation was initially performed using a coarse mesh. The number of elements was then doubled until there was no significant difference (within one percent) between the two trials as mentioned previously. The cantilever beam was modeled as shown in Figure 3.8 and the meshed model with applied boundary conditions is shown in Figure 3.9.

The modal analysis was performed for the first two modes of the cantilever beam with the aim of comparing the measurement sensitivities between the two modes. The two mode shape obtained from ANSYS are shown in Figures 3.10 and 3.11 respectively.

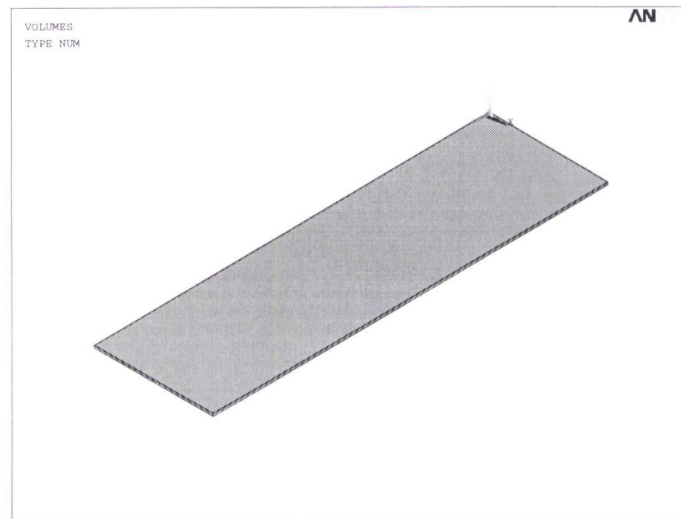


Figure 3.8: A cantilever beam modelled in ANSYS.

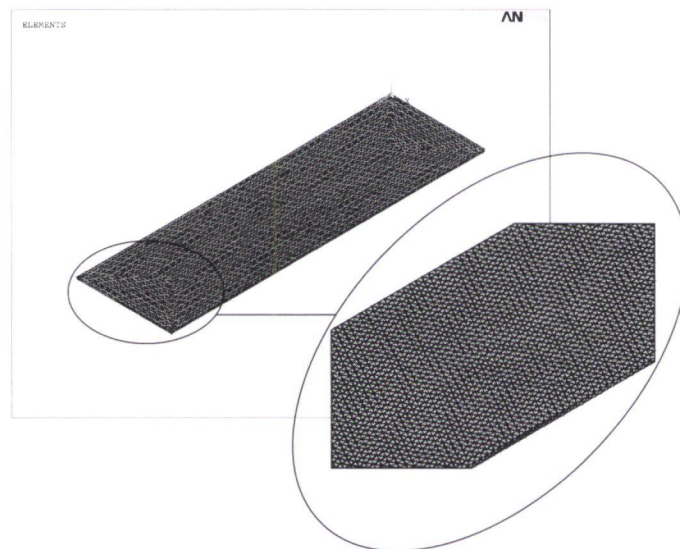


Figure 3.9: A cantilever beam meshed using SOLID95 elements. The nodes on the left hand side were fixed and a distributed pressure was applied on the top surface of the beam to represent the distributed electrostatic force.

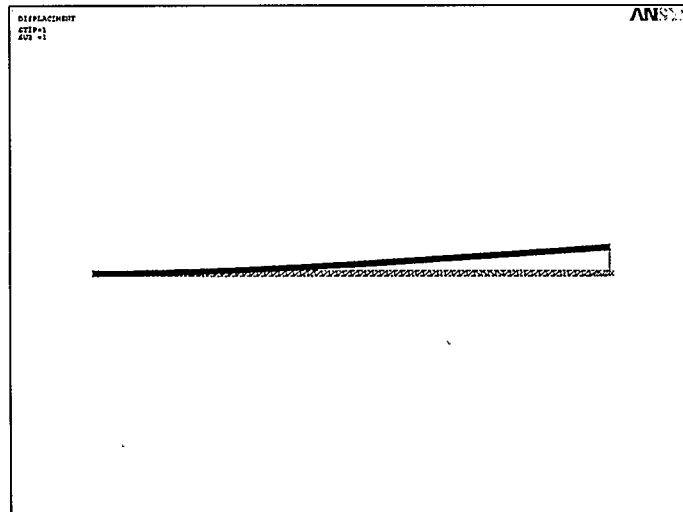


Figure 3.10: The first mode of vibration.

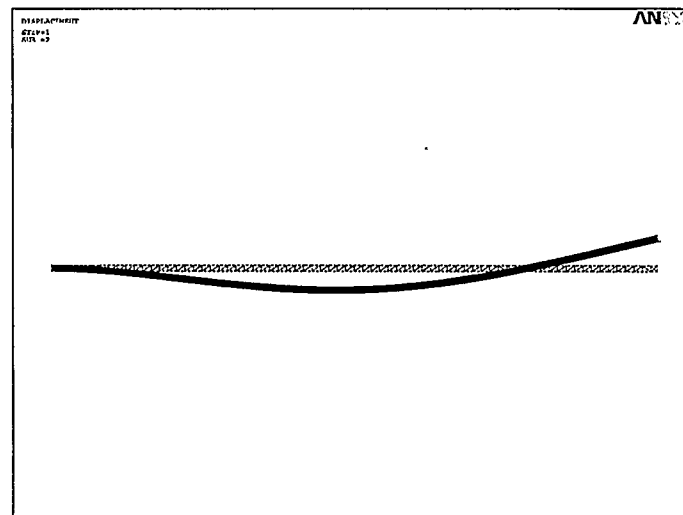


Figure 3.11: The second mode of vibration.

Thickness (nm)	Analytical f_o (KHz)	ANSYS f_o (KHz)
20	1116.065	1115.1
30	1674.097	1669
40	2232.13	2223.8

Table 3.1: The resonant frequency variation with the thickness of the beam. The width was fixed at $1.5\mu\text{m}$ and the length was fixed at $5\mu\text{m}$

To account for fabrication tolerances, the width, thickness and length of the beam were varied around the nominal dimensions to study the effect of these variations on the resonant frequency. The mask fabrication tolerance was taken to be $0.25\mu\text{m}$ which is close to what most modern MEMS fabrication facilities can guarantee and the thickness accuracy was taken to 10nm. The results were then compared to the analytical approximations obtained by Rayleigh's method in the previous chapter. The results are summarized in Tables 3.1, 3.2 and 3.3. Table 3.1 shows the resonant frequency of the beam as a function of varying thickness and Tables 3.2 and 3.3 shows the resonant frequency as a function of varying length and width respectively. Similar analysis was performed for the second mode with similar results, but for brevity, only the first mode is tabulated.

From the results it can be seen that Rayleigh's approximation is a good resonant frequency approximation and can be used as a design equation at least to the first order approximation. The tables also gives some perspective on the effect of fabrication tolerances on the resonance frequency. For example, it is very difficult to control the deposition or etching of a material in the nanometer scale, but for the dimensions of the beams dealt in MEMS design, a variation in deposition (thickness of the beam) of 10nm will cause a very significant change in the resonant frequency of the beam. Hence precise profilometry of the structure is very important to determine the exact dimensions.

Once static and modal analysis are completed, harmonic analysis can be performed. Figure 3.12 shows the harmonic response of the beam at two different beam locations. The free end of the beam has the highest amplitude for the first mode while at the center of the beam, the two modes have similar amplitudes.

Length (μm)	Analytical f_o (KHz)	ANSYS f_o (KHz)
4.75	1855.173	1850
5	1674.097	1669
5.25	1518.720	1512.9

Table 3.2: The resonant frequency variation with the length of the beam. The width was fixed at $1.5\mu\text{m}$ and the thickness was fixed at 30nm

Width (μm)	Analytical f_o (Hz)	ANSYS f_o (Hz)
1.25	1674.097	1666.7
1.5	1674.097	1669
1.75	1674.071	1670.4

Table 3.3: The resonant frequency variation with the width of the beam. The length was fixed at $5\mu\text{m}$ and the thickness was fixed at 30nm

3.4.1 Resonant Frequency Shift Due to Mass Change

To determine the change in resonant frequency of the beam as a function of the added mass, a small object representing the mass of a typical bioparticle was added at the end of the beam as shown in Figure 3.13. An add operation was used in ANSYS which ensures that the object is attached to the beam. This operation merges the different volumes into a single volume. Note that if the cantilever and the loaded mass are not added, then ANSYS solves for the modal deformation of the two bodies independently of each other giving erroneous results. The change in mass for both modes was found to be very close to the analytical expressions given in Chapter 2 as shown in Figures 3.14 and 3.15 for the first and the second mode respectively. Note that the analytical approximation results in higher resonant frequencies as expected due to overestimation of the stiffness of the beam.

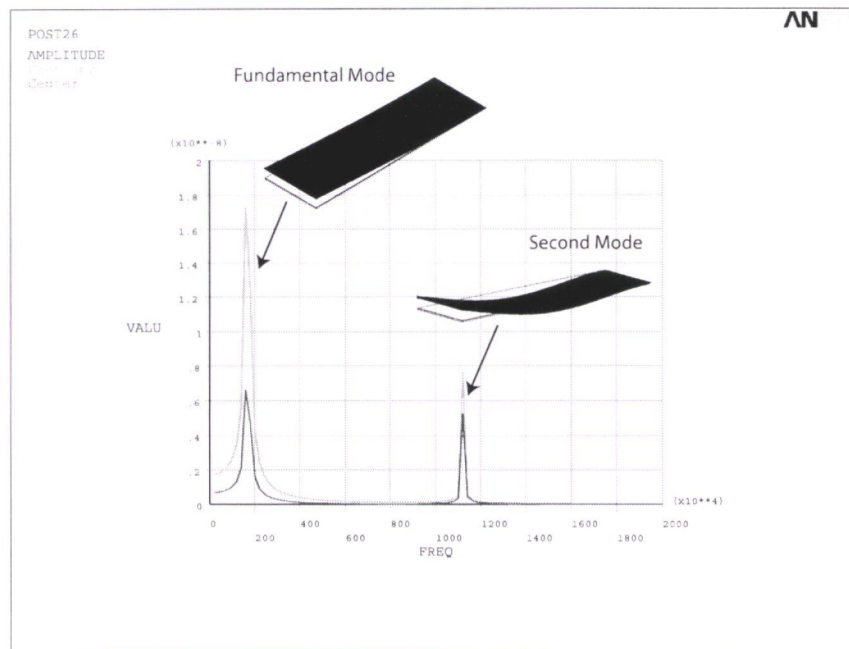


Figure 3.12: Harmonic analysis performed in ANSYS at two different points on the beam.

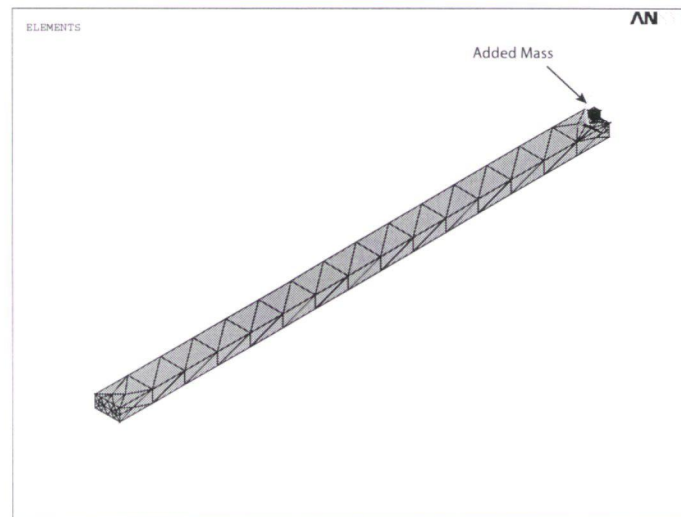


Figure 3.13: The cantilever beam with a mass loaded at the free end. The beam used had the dimensions of $L = 40\mu\text{m}$, $T = 1\mu\text{m}$ and $w = 2\mu\text{m}$.

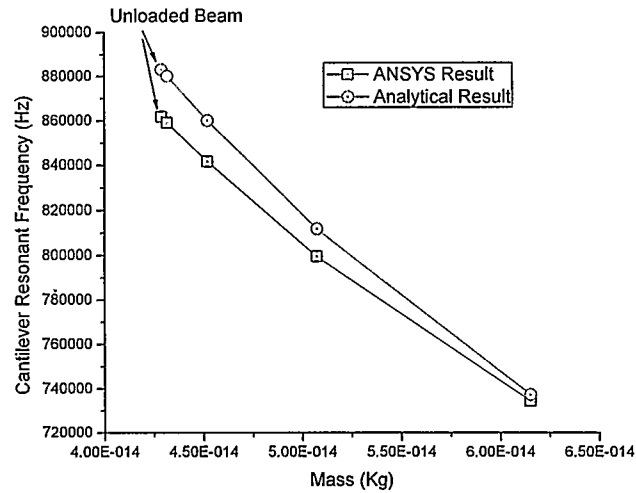


Figure 3.14: Comparison between the ANSYS simulation for the effect of mass loading on the first mode resonant frequency and the analytical expression given by Equation 2.65 from Chapter 2.

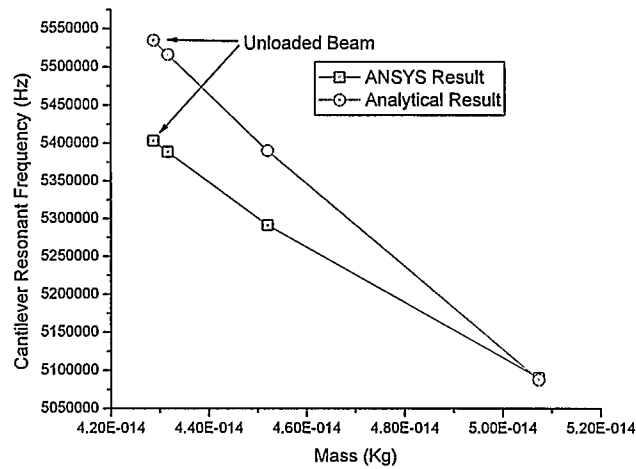


Figure 3.15: Comparison between the ANSYS simulation for the effect of mass loading on the second mode resonant frequency and the analytical expression given by Equation 2.66 from Chapter 2.

When the cantilever is used as a bioparticle detector, it is impractical to assume that the particle will be at the end of the beam since in reality, the particle may randomly fall anywhere on the surface of the beam. Therefore, it is important to minimize the measurement sensitivity to the particle placement on the beam. The next section looks at the effect of this positioning and it is shown that the second mode is less sensitive and hence provides an opportunity for more accurate measurement compared to the first mode.

3.5 Mass Placement Dependence on the Vibration Modes

It was mentioned before that the second mode has an advantage over the first mode in terms of the measurement sensitivity to the mass placement location on the beam. This can be shown analytically using the stiffness and mass matrices calculated by the finite element method [36]. Note that by moving the mass around on the surface of the beam, the dynamic parameter that we are changing is the stiffness matrix. Ignoring damping, a dynamic system can be represented in matrix form as [36]

$$-\omega_o^2[M][\Phi] + [K][\Phi] = 0 \quad (3.7)$$

where ω_o is the resonant frequency, $[M]$ is the mass matrix, $[K]$ is the stiffness matrix and $[\Phi]$ is the mode shape. To see the effect of moving the mass around, we perturb the matrix $[K]$ by a small value ΔK and see the effect this has on the resonance frequency. Perturbing $[K]$ will also change the mode shape Φ and we have

$$-(\omega_o + \Delta\omega_o)^2[M]([\Phi] + \Delta[\Phi]) + ([K] + \Delta[K])([\Phi] + \Delta[\Phi]) = 0 \quad (3.8)$$

Multiplying throughout by the mode shape transpose $[\Phi]^T$ and solving for the frequency change $\Delta\omega_o$, we get

$$\Delta\omega_o = -\frac{1}{2} \frac{(-\omega_o^2[M] + [K])\Delta[\Phi] + [\Phi]^T \Delta[K][\Phi]}{\omega_o[\Phi]^T[M][\Phi]} + O(2) \quad (3.9)$$

where $O(2)$ are the second and higher order terms. Ignoring the higher order terms and dividing throughout by ω_o , we get

$$\frac{\Delta\omega_o}{\omega_o} = -\frac{1}{2} \frac{(-\omega_o^2[M] + [K])\Delta[\Phi] + [\Phi]^T \Delta[K][\Phi]}{\omega_o^2[\Phi]^T[M][\Phi]} \quad (3.10)$$

Since the stiffness and mass matrices are symmetric, the following relationship holds [36]

$$[[\Phi]^T(-\omega_o^2[M] + [K])]^T = (-\omega_o^2[M] + [K])[\Phi] = 0 \quad (3.11)$$

Therefore, the resonance frequency shift expression simplifies to

$$\frac{\Delta\omega_o}{\omega_o} = \frac{1}{2} \frac{[\Phi]^T \Delta[K][\Phi]}{\omega_o^2[\Phi]^T[M][\Phi]} \quad (3.12)$$

From Equation 3.12, it can be seen that the change in resonance frequency due to perturbation in the stiffness matrix is inversely proportional to the square of the resonance frequency. Since the resonance frequency for the second mode is about 6 times the resonance frequency for the first mode, the second mode is roughly 36 times less sensitive to mass placement as compared to the first mode.

3.6 Viscous Damping

To characterize viscous damping in ANSYS, the fluid dynamics module was used to model the fluid surrounding the cantilever beam. ANSYS fluid dynamics module solves the incompressible Navier-Stokes equations which can be written in vector form as [3]

$$\rho \frac{\partial \vec{u}}{\partial t} + \vec{u} \bullet \nabla \vec{u} = \delta \nabla^2 \vec{u} - \nabla p + f \quad \text{Momentum Balance} \quad (3.13)$$

$$\nabla \bullet \vec{u} = 0 \quad \text{Mass Balance} \quad (3.14)$$

where \vec{u} is the fluid velocity vector, ρ is the fluid density, δ is the fluid viscosity, p is the fluid pressure and f is the source term.

3.6.1 Arbitrary Lagrangian Eulerian (ALE) Formulation

Numerical algorithms for continuum mechanics usually make use of two classical description of motion [3]. These are the Lagrangian description where the observer can be thought of as being inside the moving body and the Eulerian description where we have an external observer observing the motion. In terms of the mesh description of a moving or deforming body, the Lagrangian mesh can deform (the mesh follows the moving body) while the Eulerian mesh is fixed (the mesh solves for whatever passes through it). Figures 3.16 and 3.17 illustrates a one-dimensional example of the Lagrangian and Eulerian descriptions of motion respectively [3].

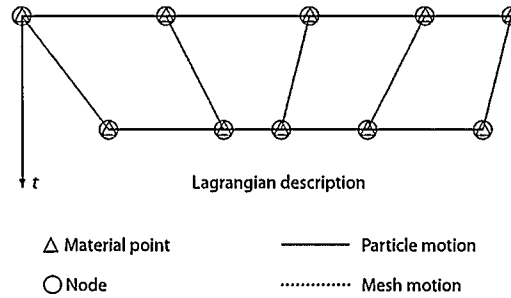


Figure 3.16: One dimensional illustration of the Lagrangian description of motion. The mesh moves with the body [3].

Both methods have their advantages and disadvantages. However, in fluid mechanics, the method of choice is Eulerian description since it can handle large distortion in the continuum with relative ease. Since the mesh is fixed for the Eulerian description, moving boundaries can not be handled with the standard fluid mechanics algorithms. A new technique called Arbitrary

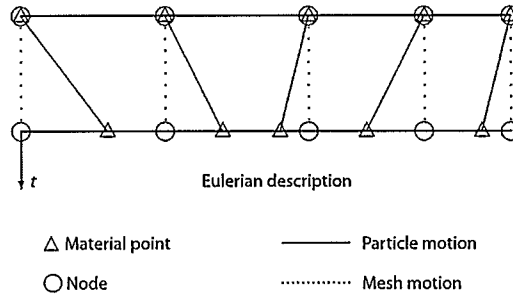


Figure 3.17: One dimensional illustration of the Eulerian description of motion. The mesh is stationary relative to the body [3].

Lagrangian Eulerian (ALE) combines the two descriptions of motions allowing the ease of use of the Eulerian description as well as accommodating moving boundaries. Moving boundaries are essential for studying fluid-structural interaction since the fluid boundary can be dynamic and the effects of the boundary motion can be studied. ANSYS supports the ALE formulation and it will be used to study the effect of fluid on the oscillating cantilever beam. For further details of the ALE technique, the reader is referred to Donea et. al. [3].

3.6.2 Damping Coefficient Extraction

To extract the damping coefficient using a finite element method, first it is beneficial to understand the basic technique applicable to rigid bodies. For rigid bodies, all nodes of the structure move together and hence the formulation only needs to take into account the movement of the nodes with respect to time. As each node is always at the same place relative to other nodes, there is no need for spatial description of the nodal motion. A three dimensional fluid volume can be simulated using FLUID142 element with the ALE option turned on. FLUID142 is a 3-dimensional fluidic element that supports the ALE formulation and therefore it can be used for solving fluid-solid interaction problems. One of the fluid boundaries is fixed and the other one is oscillated at the resonant frequency of the beam. To obtain the damping coefficient, consider Figure 3.18. If the oscillating beam is moving in a sinusoidal fashion expressed as

$$z = z_o \cos \omega t \quad (3.15)$$

then the velocity and the acceleration are given as

$$\dot{z} = -z_o \omega \sin \omega t \quad (3.16)$$

and

$$\ddot{z} = -z_o \omega^2 \cos \omega t \quad (3.17)$$

respectively.

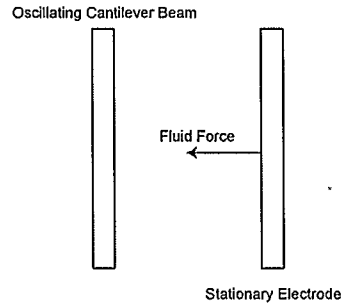


Figure 3.18: An oscillating beam experiencing fluid force from the surrounding fluid.

Since the motion of the beam is sinusoidal, the fluid force will also have a sinusoidal form [37] and can be written as

$$F_{fluid} = F_o \cos(\omega t + \varphi) \quad (3.18)$$

where φ is the phase difference between the motion of the beam and the fluid response. Expanding the cosine relationship, we have

$$F_{fluid} = F_o \cos \omega t \cos \varphi - F_o \sin \omega t \sin \varphi \quad (3.19)$$

If the driving electrostatic force is denoted as $F_{driving}$, then the force balance equation is

$$M\ddot{z} + F_{fluid} = F_{driving} \quad (3.20)$$

Substituting Equation 3.19 into Equation 3.20, we get

$$M\ddot{z} + F_o \cos \omega t \cos \varphi - F_o \sin \omega t \sin \varphi = F_{driving} \quad (3.21)$$

From Equations 3.15 and 3.16, we can express the sinusoid functions in terms of the displacement and velocity as

$$\cos \omega t = \frac{z}{z_o} \quad (3.22)$$

and

$$\sin \omega t = -\frac{\dot{z}}{z_o \omega} \quad (3.23)$$

Substituting these values into Equation 3.21, we obtain the equation of motion in a standard form

$$M\ddot{z} + \left(\frac{F_o \sin \varphi}{\omega z_o} \right) \dot{z} + \left(\frac{F_o \cos \varphi}{z_o} \right) z = F_{driving} \quad (3.24)$$

Hence the damping factor, which is the velocity coefficient, can be obtained by finding the phase difference φ . φ can be determined by plotting the displacement of the beam and the fluidic response on the same graph. Note that the stiffness of the beam is also affected by damping due to the displacement coefficient given by

$$\frac{F_o \cos \varphi}{z_o} \quad (3.25)$$

This effect is frequency independent and it will add directly to the original structural stiffness.

Figure 3.19 shows the plot of a typical beam displacement and the fluid pressure as a function of time for the first mode. The plot can be used to extract the value of the phase difference φ . This value is then substituted in Equation 3.24 to solve for the damping coefficient.

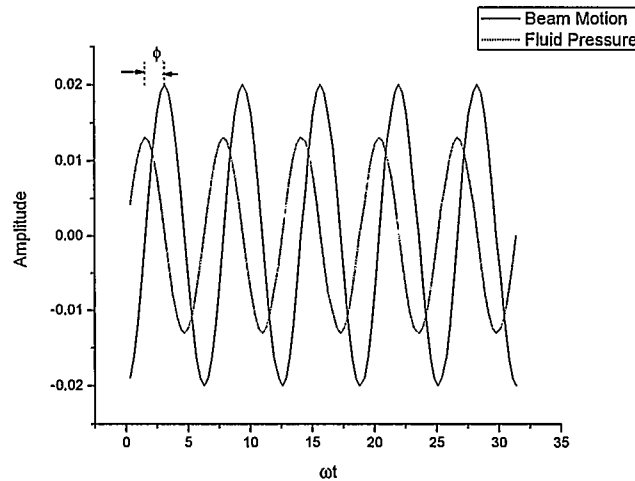


Figure 3.19: Plot of the beam displacement and the fluid pressure used to determine the phase difference φ .

However, for an elastic structure like the cantilever beam, the relative position of a given node relative to other nodes changes as the body deforms. Therefore, the formulation of the problem has to include the temporal as well as spatial information about the node. Inclusion of the spatial information is very complicated and there is no general way of doing it [38]. One way of doing it is to use mode shapes as described in Chapter 2, which is only applicable to linearized equations. For a linearized Reynold's equation governing squeeze film damping, a modal projection technique (where the fluidic forces are expressed in modal coordinates) has been implemented in ANSYS version 8.1 as FLUID136. The problem is defined by creating a structure using 3-D solid elements

(for example, SOLID45) and attaching a corresponding FLUID136 element on each solid element such that the nodes at the boundary coincide. This is shown in Figure 3.20.

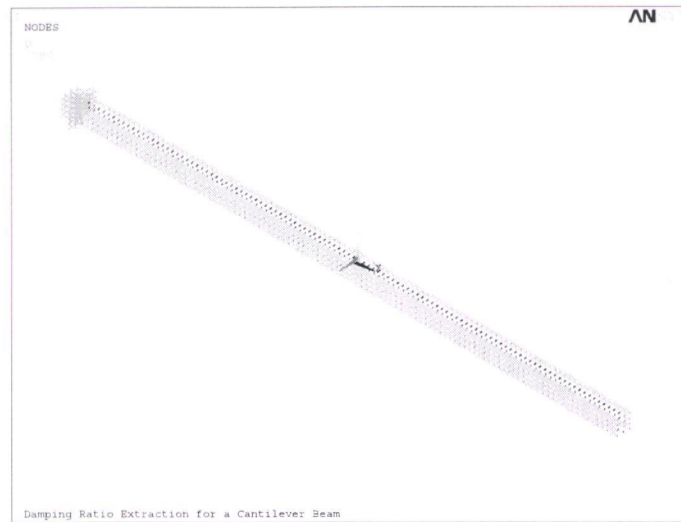


Figure 3.20: FLUID136 nodes on top of SOLID45 nodes. The nodes have to coincide at the boundary.

ANSYS first solves for the mode shapes of interest. This is exactly the same as the modal analysis described previously. Once the mode shapes are known, they are then used to excite the squeeze film model (FLUID136 elements) in the whole frequency range specified to determine the frequency response [38]. Figures 3.21 and 3.22 shows the modal excitement for modes 1 and 2 respectively.

The pressure values are then calculated for each mode. Once the pressures for each FLUID136 element are known, they are integrated to compute the force vector for each frequency. The scalar

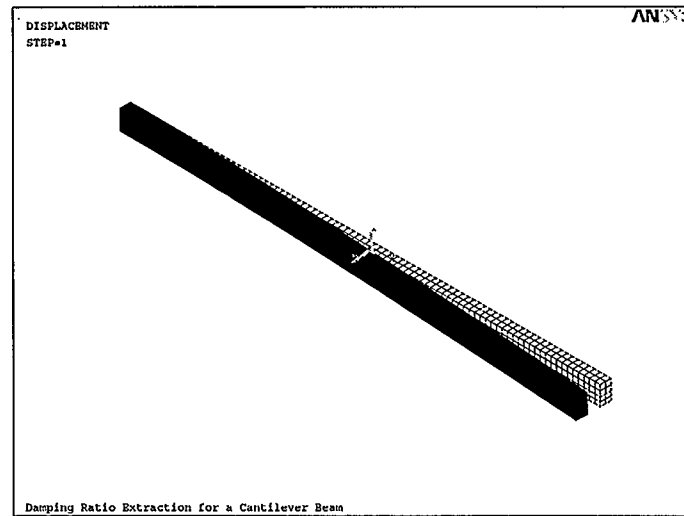


Figure 3.21: The FLUID136 element excited using the first mode shape.

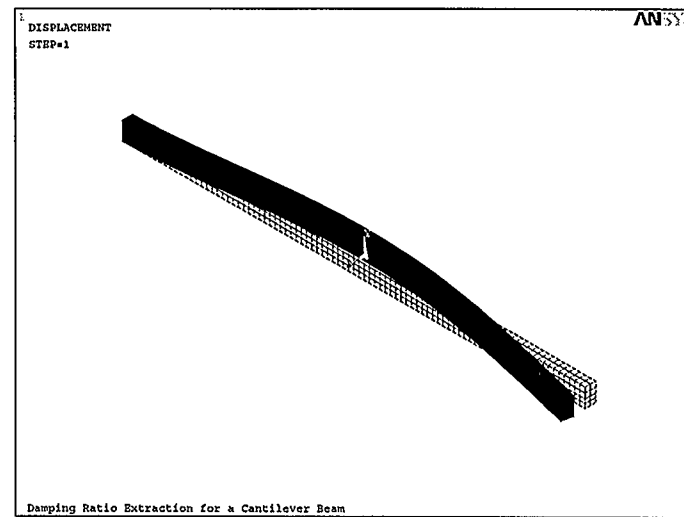


Figure 3.22: The FLUID136 element excited using the second mode shape.

products of all force vectors are then computed — the scalar products represents the modal forces and they state how much of the pressure distribution acts on each mode. The pressure can be used to determine two matrices; the modal damping coefficient matrix C_{ij} and the modal squeeze stiffness matrix K_{ij} . The subscript i represents the deflection mode (source mode) while subscript j represents the mode experiencing the pressure (target mode). The diagonal terms of the matrices represent the coefficients for each mode while the off-diagonal terms represent the cross-talk between modes [39]. The damping ratio ξ_i for mode i can be obtained from the matrix coefficient C_{ii} as

$$\xi_i = \frac{C_{ii}}{2\omega_i m_i} \quad (3.26)$$

where ω_i is the resonant frequency of mode i and m_i is the modal mass.

This analysis was performed for the cantilever beam with the same dimensions as in previous discussions and the results were compared to the approximation based on the simplified Reynold's Equation from Chapter 2. A variation of several parameters was performed and the comparison between the two results plotted. Figure 3.23 shows the damping ratio as a function of resonant frequency of the beam for the first mode. It can be seen that the higher the resonant frequency, the smaller the damping factor as predicted by the simplified Reynold's equation. The resonant frequency of the beam was varied by changing the thickness of the beam. This has no effect on the squeezed film since the surface of the beam interacting with the fluid remains the same.

However, if we change the width of the beam, we expect the damping to vary accordingly since now the beam area squeezing the film is changing. Figure 3.24 shows the same plot for a beam that is 5 times as wide compared to the results plotted in Figure 3.23. It can be seen that the trends are similar for both analytical and ANSYS results. However, the values of damping ratio are an order of magnitude higher. This increase in damping is expected since a wider beam has more surface interacting with the fluid leading to more energy dissipation.

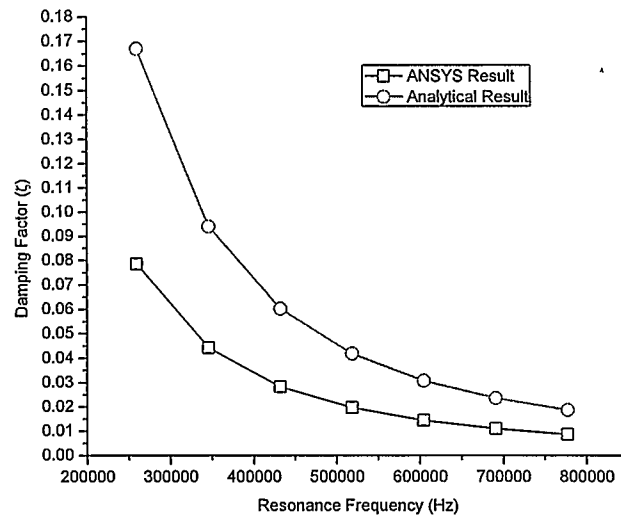


Figure 3.23: The damping ratio as calculated by an analytical approximation based on simplified Reynold's equation compared to the value calculated by ANSYS. The horizontal axis represents the cantilever resonance frequency. The beam simulated has the width of $2\mu\text{m}$, length of $40\mu\text{m}$ and thickness of $1\mu\text{m}$.

Figure 3.25 shows the variation of the damping with the gap. Again, as expected, the larger the gap the smaller the damping. Figure 3.26 shows the comparison for the second mode of vibration. It can be seen that the simplified Reynold's equation provides a good first-order approximation for damping even for higher modes of vibration. Note that for all the simulations the ANSYS results are smaller than the values predicted by Reynold's equation. This can be explained by referring to Figure 3.27. Reynold's equations assumes rigid body motion for the cantilever beam as shown on the right of the figure while in reality the cantilever deforms into the different mode shapes. The figure shows the deformation for the first mode. It is apparent that for a rigid body approximation, damping is overestimated since more beam area squeezes the fluid film than what actually happens. Similar arguments apply to higher modes of vibration.

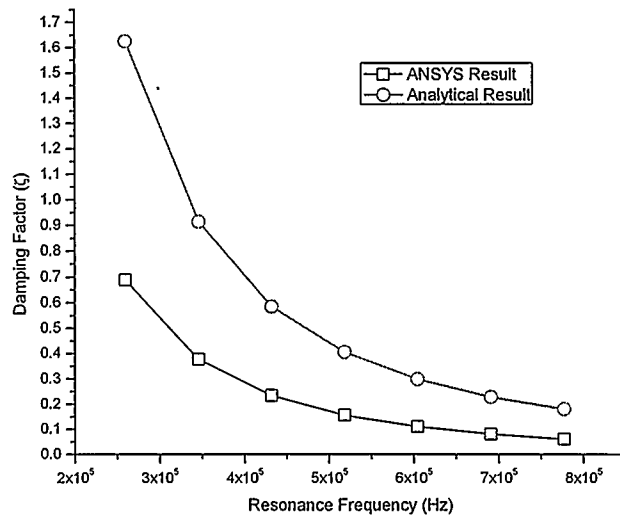


Figure 3.24: Comparison between the analytical and ANSYS results for the damping ratio for a beam that is $10\mu\text{m}$ wide with other dimensions as the beam in Figure 3.23.

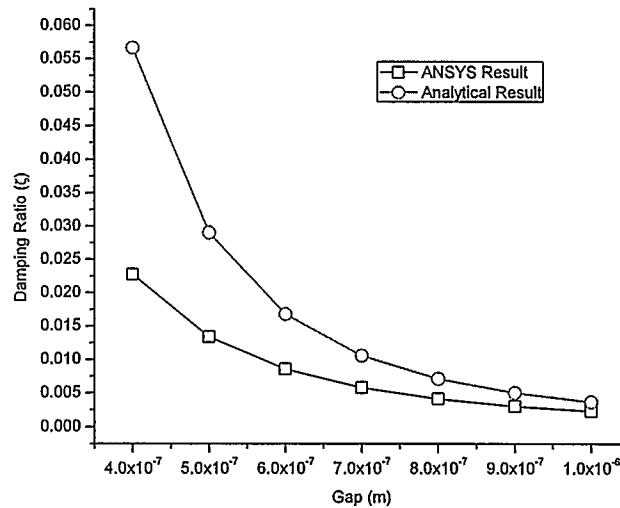


Figure 3.25: Comparison between the analytical and ANSYS results for the damping ratio for a beam as a function of the gap.

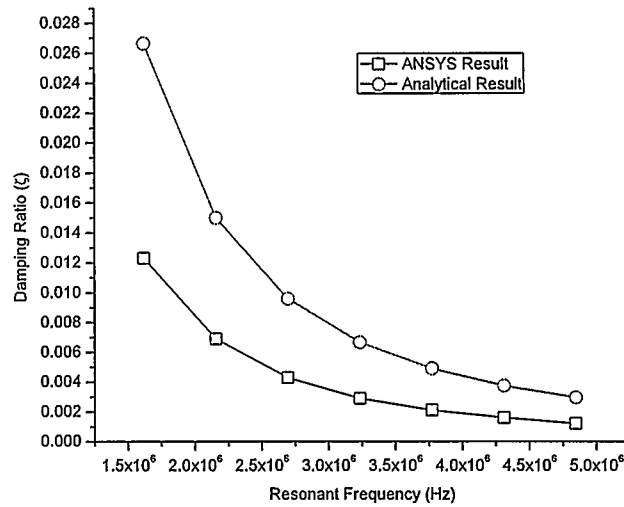


Figure 3.26: Comparison between the analytical and ANSYS results for the damping ratio for a beam for the second mode. The dimensions used are the same as those for Figure 3.23.

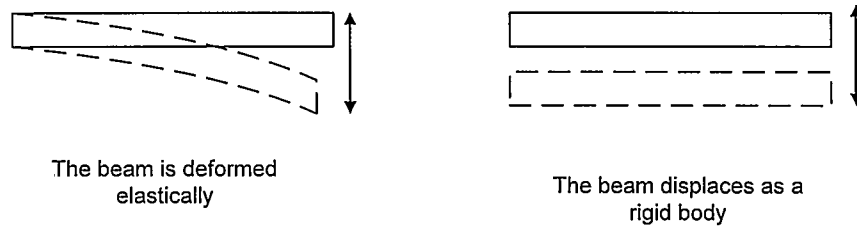


Figure 3.27: The analytical Reynold's equation assumes rigid body deformation as shown on the right. The actual displacement is as shown on the left for the first mode covering less area between the moving surface and the fluid. Hence, the actual damping is less than the one predicted by the analytical Reynold's equation.

As mentioned before, the fluid forces can behave as a damping or stiffness effect depending on the frequency of vibration of the cantilever beam. At low frequencies, the fluid can track the beam by going back and forth as the beam oscillates, hence the force is proportional to the beam velocity acting as a damper. However, at higher frequencies, the fluid can not move with the beam

and it acts as a spring increasing the effective stiffness of the beam. It is important to determine these effects accurately so that they can be included in the design process. ANSYS can be used to calculate these values as shown in Figure 3.28. The cantilever beam resonant frequency is shown on the figure and at that frequency the damping is still dominant and the fluid stiffness adds an extra 5% to the structural stiffness.

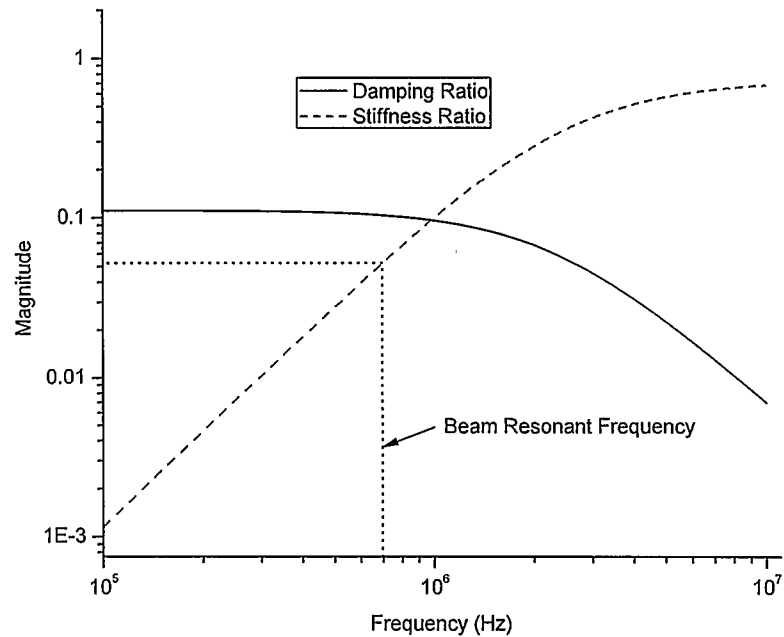


Figure 3.28: The damping ratio plotted with stiffness ratio as a function of frequency. The stiffness ratio describes how much the fluidic stiffness contributes to the overall structural stiffness. In this case, at resonance we have a ratio of roughly 0.05 which means the fluidic stiffness adds an extra 5% to the structural stiffness.

It is also interesting to look at how this phenomenon depends on the viscosity of the fluid. The value of viscosity used to obtain results in Figure 3.28 was the typical value of air viscosity at room temperature which is $1.85 \times 10^{-5} \text{ Kg/m} \cdot \text{s}$. To study how viscosity affects the damping and fluid stiffness characteristics, another simulation was performed with ten times as much viscosity.

The comparison is shown in Figure 3.29. The original results (same as Figure 3.28) are shown with the triangular points. Two observations can be made concerning the high viscosity results. First, even though the trends of the damping and fluid stiffness are similar to the lower viscosity results, the crossover from dominant damping to dominant fluid stiffness occurs at a much lower frequency. Intuitively, this can be explained by the fact that the more viscous the fluid, the harder it is for it to follow the oscillating cantilever beam and the cut-off frequency where it turns into an effective spring is lower than for a less viscous fluid. The second observation is that when viscosity is higher, both damping and fluid stiffness are higher creating more energy dissipation in the whole frequency range of operation.

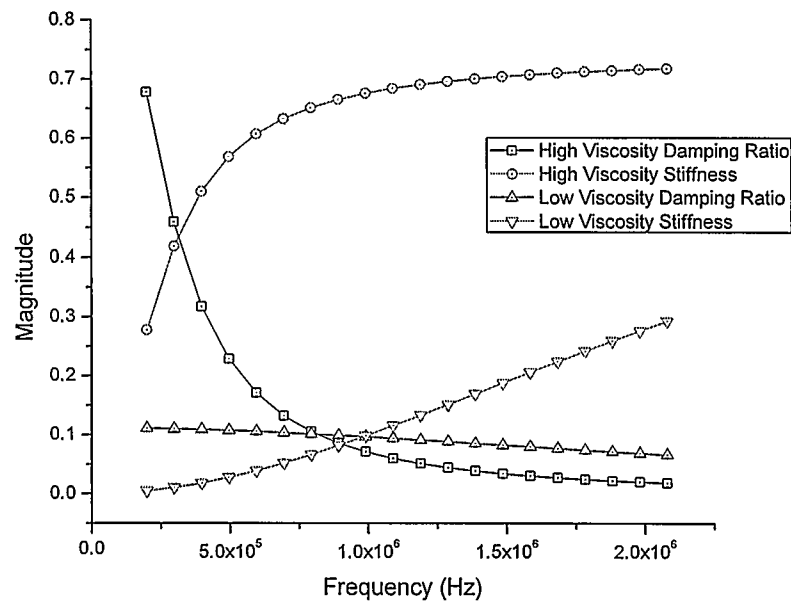


Figure 3.29: The effect of fluid viscosity on the damping ratio and fluid stiffness as a function of frequency.

In the next chapter, techniques for extracting parameters to allow for system level simulations

will be discussed. The damping values obtained in this section will be directly used in the system level models.

Chapter 4

System Level Modeling

This chapter describes the highest level of abstraction in the modeling hierarchy described in Chapter 1. A technique called reduced order modeling (ROM), where infinite degrees of freedom are reduced to a few dominant degrees of freedom is introduced. ANSYS supports the ROM for electrostatic-structural transducers and the specific element for this task is described. The element generates the ROM which can be used within ANSYS for very simple system level modeling or exported in a VHDL-AMS language which allows the ROM to be used in more sophisticated external system simulators. Simulation results for damped harmonic response were performed within ANSYS and these are compared with full FEM results. A short introduction to the VHDL-AMS is then given. The VHDL-AMS code generated by ANSYS is subsequently analyzed. Due to time constraints, the VHDL-AMS code was not used, but some of the lumped parameters were utilized in a Simulink simulator to design a Q -controller based on a velocity feedback technique.

4.1 Reduced Order Modeling (ROM)

Transducers, by definition, involve multiple energy domains. As described in the previous chapters, the cantilever sensor involves kinetic energy, elastic deformation, electrostatic energy and fluidic interactions. It is very useful to capture the complex multi-physics domains in relatively compact dynamic models [40, 41] for two main reasons. By having accurate compact models, the dynamic simulations can be performed much more rapidly compared to the finite element simulations. Secondly, and more importantly, the captured models can be connected to other system components allowing a system level simulation and performance evaluation. This is paramount for MEMS since the mechanical structures are usually connected to electronics. These captured models are usually called reduced order models (ROM) because of the relatively few dynamic degrees

of freedom, very similar to the description in Chapter 2.

The requirements for the ROM are [40]:

- Analytical rather than numerical.
- Correct dependence on the device dimensions and material properties.
- Correct energy behavior — conserving or dissipating.
- Acceptable quantitative agreement with full FEM simulations and experimental results.

The process of obtaining the ROMs is usually a full run of FEM to solve for the particular modes of interest. Once the relevant modes are known, the input/output relationship of the transducer can then be expressed using SPICE models or VHDL-AMS language. SPICE models can be used in circuit simulators, while VHDL-AMS models allow for system level simulation. Specific ROM capabilities of the ANSYS software will be described next.

4.2 ROM in ANSYS

ANSYS 8.1 provides an interface for exporting the coupled electrostatic/structural interaction solution to a VHDL-AMS model through the element ROM144. The element is described and some theoretical background on the generation of the element data is provided.

4.2.1 The ROM144 Element

ROM144 can be used to represent either a 2-D or a 3-D reduced order model of a coupled electrostatic-structural system [42]. The element has nine modal degrees of freedom and five voltage degrees of freedom. A typical sequence for generating the ROM is shown in Figure 4.1. The first step is to create the FEM model as described in the previous chapter. Since ROM144 couples two domains (electrostatic and structural), the meshing, material properties and boundary conditions have to take this into account. Once the FEM model is ready, the so-called “generation” pass is

performed to solve the FEM model and generate the ROM144 element. This element can either be used within ANSYS with other ROM elements or it can be exported into a VHDL-AMS code. In this work, harmonic analysis is performed within ANSYS and the results are compared with a full finite element solution.

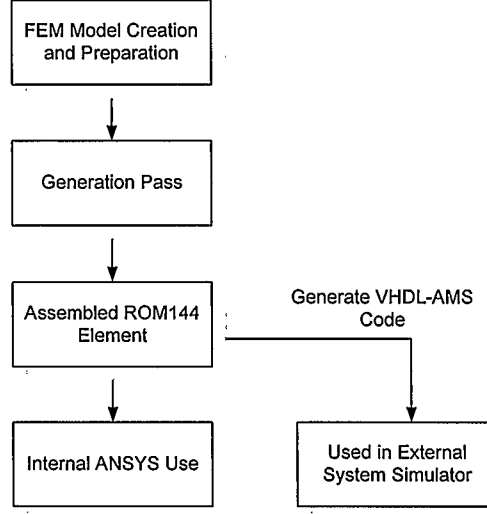


Figure 4.1: The ROM144 generation process.

Reduced order modeling of coupled domains is based on the principle of normal coordinate transformation as described in Chapter 2 [42]. The deformation state u of the structure is expressed as a sum of weighted mode shapes

$$u(x, y, t) = u_{eq}(x, y) + \sum_{i=1}^m q_i(t) \Phi_i(x, y) \quad (4.1)$$

where q_i is the modal amplitude of mode i as a function of time, Φ_i is the mode shape, u_{eq} is the equilibrium deformation and m the number of modes of interest. By substituting Equation 4.1 into the second order system, we obtain m equations that describe the structural domain in modal coordinate as [42]

$$m_i \ddot{q}_i + 2\xi_i \omega_i m_i \dot{q}_i + \frac{\partial W_{SENE}}{\partial q_i} = \sum F \quad (4.2)$$

where m_i is the modal mass, ξ_i is the modal damping factor, ω_i is the angular frequency, W_{SENE} is the strain energy and $\sum F$ is the total external force applied. Note that the partial derivative is the derivative of energy per displacement and therefore it has the unit of force consistent with the rest of the parameters. For linear structural systems, the derivative can be simplified to the stiffness constant multiplied by displacement, but in general, the strain energy depends on the generalized coordinates q_i . When coupled with electrostatic system, the electrostatic force in the modal domain is given by [42]

$$\frac{1}{2} \frac{\partial C_{ij}}{\partial q_i} (V_i - V_j)^2 \quad (4.3)$$

where C_{ij} is the capacitance between conductors i and j and V is the potential at a given conductor.

4.2.2 Damped Harmonic Response

By now, it is apparent that the damped harmonic response is a very important characteristic of the resonant mass sensors. The responses were simulated using a fully blown FEM (nodal) solution as well as using the ROM element extracted through the ROM144 element. Figure 4.2 shows the response obtained from FEM solution while Figure 4.3 shows the ROM response.

For both responses, the amplitude is of the point at the free end of the beam. It can be seen that the two responses are very similar despite the fact the FEM solution took about 4 hours to run while the ROM solution took less than a minute. This illustrates one of the advantages of the ROM technique which is an accurate but also very compact representation of the dynamics of the

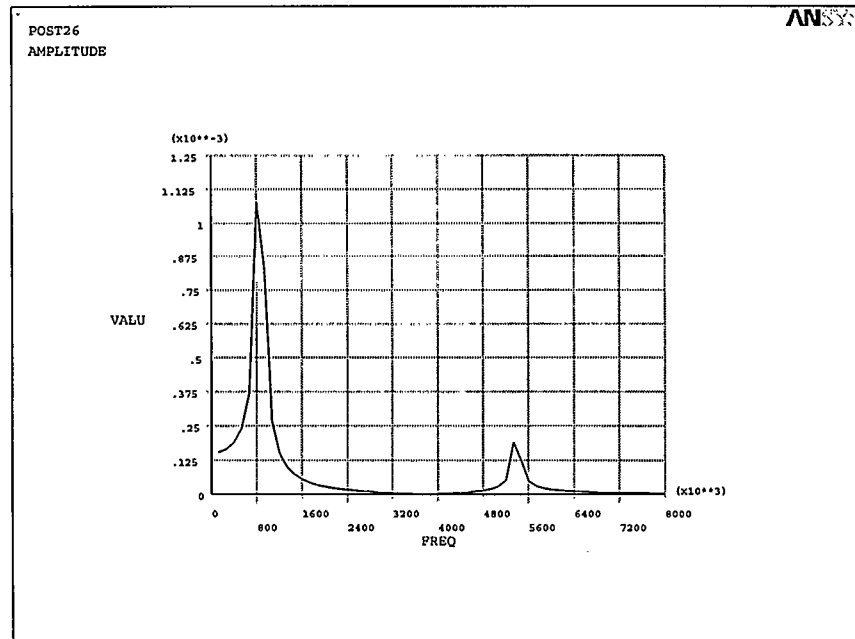


Figure 4.2: The damped harmonic response using full FEM harmonic analysis.

transducer. The other advantage is the ability to integrate the ROM with other components in a system level simulator. This is achieved through a description language VHDL-AMS which will be discussed next.

4.3 The VHDL Language

VHDL stands for **V**HSIC **H**ardware **D**escription **L**anguage, where VHSIC is an abbreviation for **V**ery **H**igh **S**peed **I**ntegrated **C**ircuit. It was developed in the eighties by a collaborative effort between the United States Department of Defense and the IEEE. The purpose of the language was to enable standardized simulation and synthesis of digital systems with many features including

- Support for hierarchical designs.
- Each design element has a well defined interface (for interconnection) and a precise behavioral specification (for simulation).

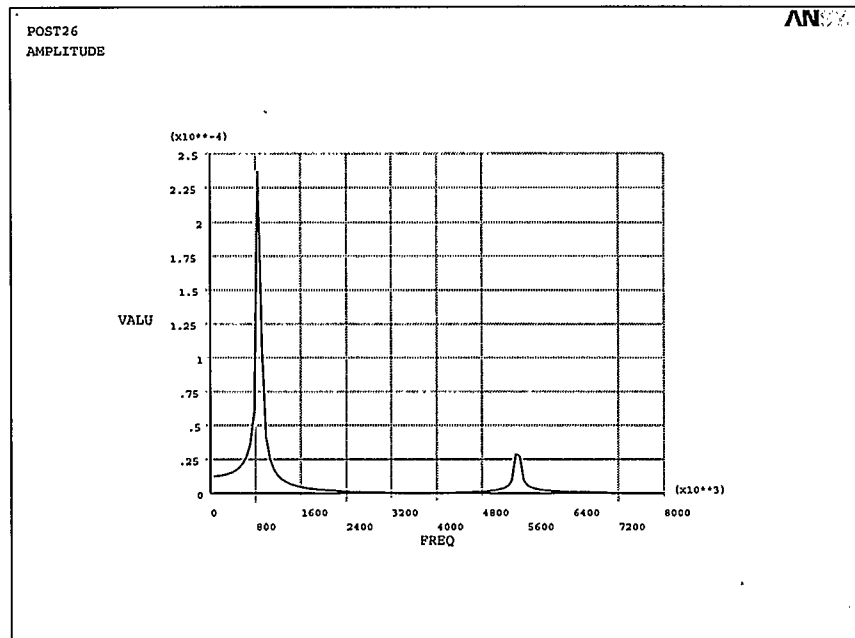


Figure 4.3: The damped harmonic response using the ROM. The ROM was used within the ANSYS environment.

- Allows concurrent simulation.
- Hardware can be synthesized directly from algorithms.

Typical structure of VHDL code is shown in Figure 4.4. There are two main sections. The entity section defines how the device described by the VHDL code interfaces with external parameters. When the code is used in system level simulation, the user of the device does not need to know its internal workings, but rather just understand the interface definitions. The second portion of the code, known as the architecture, is what defines the behavior of the device.

VHDL has grown dramatically. Now there is a standard implemented in many commercial tools, enabling digital designers to develop complicated systems more rapidly and reliably relative to what was achievable with schematics-based development tools of the earlier era. Recently,

```

entity sensor is
    description of sensor interface
end entity sensor

architecture ideal of sensor is
begin
    sensor_behavior:process is
        begin
            description of sensor behavior
        end process sensor_behavior
    end architecture ideal

```

Figure 4.4: General outline of VHDL code.

an extension to VHDL known as VHDL-AMS (for Analog and Mixed Signals) has been developed. This extension adds the ability to simulate analog and mixed (analog/digital) signals as well as variables from other domains (including mechanical, fluidic and thermal). Commercial tools supporting VHDL-AMS have started appearing even though they are not very well established. Since VHDL-AMS supports multiple domains, it is ideal for MEMS (and transducers in general) modelling and simulation. The following subsection describes the VHDL-AMS code generated by ANSYS.

4.3.1 VHDL-AMS Code

From a MEMS designer's point of view, the most important addition to the VHDL language is the ability to simulate variables in domains other than electrical. An IEEE standard has been proposed for VHDL-AMS and it includes the variables from different physical domains. In terms of other language constructs, VHDL-AMS is similar to most programming languages, in that it includes the ability to create loops, case statements, if-else statements and creation of functions. For further details, the reader is referred to [43].

Once the ROM144 generation pass is performed, ANSYS exports four VHDL files. The main file is called *transducer.vhdl*. This file contains the entity and behavior definition of the device. It also has the function *spoly_calc* which calculates the polynomial representations of the device based on the extracted capacitance and strain energy. The file beginning with *cal2_ams* contains

the extracted capacitance information while the file beginning with *s_ams* contains the strain energy information. The fourth file is called *initial.vhdl* which contains the initial values of the variable used in the main file. The complete generated code is attached in Appendix A.

4.4 System Level Simulation of a Q -Controlled Sensor

Due to time constraints and the unavailability of a fully featured VHDL-AMS simulator in the BRAG laboratory at the time being, the VHDL-AMS code generated by ANSYS was not used to perform system level simulation of the Q -controlled sensor. Instead, a lumped parameter second order system was used. This system is less accurate than the VHDL-AMS code with the main difference being the use of strain energy function in the VHDL-AMS code and a lumped constant stiffness in the second order approximation. However, as explained previously, this approximation is accurate for small displacement of the cantilever beam. The lumped system parameters were all obtained from finite element simulations with ANSYS. Effective mass and effective stiffness for each mode can be obtained in ANSYS by using the ROM technique. The effective modal damping used was the one obtained in Chapter 3. The system was implemented in Simulink dynamic simulator from Mathworks. Figure 4.5 shows the second order system implementation as given by Equation 2.28. The system is driven by a harmonic signal to study its response.

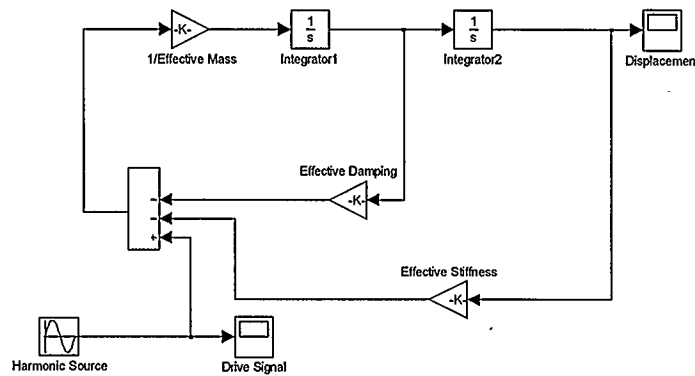


Figure 4.5: The second order system representing the cantilever beam dynamics.

The same system can also be represented using a transfer function in the s -domain. Since the transfer function is in s -domain, it represents the magnitude as well as the phase response of the system. The magnitude response is the same as the harmonic response we saw earlier and the phase response gives us information about how much the system shifts the phase of a sinusoid at a particular frequency. The block labelled “Transfer Fcn” in Figure 4.6 represents the cantilever beam system. The output of the system which is the displacement of the beam, is phase shifted and amplified as described in Chapter 2, section 4 in order to modify the damping coefficient. The effective ODE for the system is now given as

$$\ddot{z} + \left(\frac{c}{m} - \frac{G}{m\omega} \right) \dot{z} + \frac{k}{m} z = \frac{F}{m} \quad (4.4)$$

where m , c and k are the effective modal mass, damping and stiffness respectively, extracted from ANSYS. The amplified and shifted displacement is then added to the driving oscillator. Note from Equation 4.4 that the higher the frequency, the higher the gain that is required to subtract from the inherent damping. In practice, this may cause problems since the gain also amplifies noise and therefore there is a threshold gain where any additional increase will not be beneficial. Figure 4.7 compares the frequency responses for the uncontrolled and the feedback-controlled systems. It can be seen that there is significant improvement in the quality factor. Simulink was used to show the effect of feedback on damping factor. The gain used for this particular system simulation was approximately 1.3. This demonstrates that the feedback technique can have significant impact on the damping by using modest gain values. Since the velocity feedback directly affect the damping factor, its effects can also be seen by directly modifying the transfer function and plotting the analytical expression rather than numerically solving for the ODE by using Simulink. The plots using analytical transfer functions are shown in Figure 4.8.

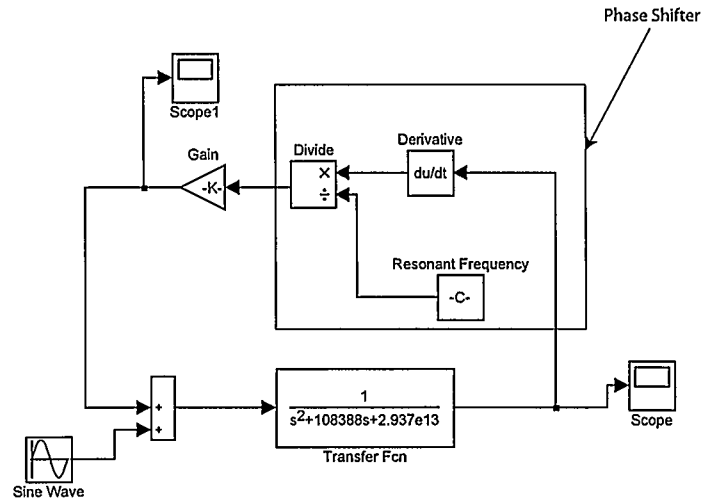


Figure 4.6: Feedback control used to reduce damping.

The following section will discuss a chip consisting of array of cantilever beams fabricated using the MUMPs process.

4.5 MUMPs-Based Chip

An array of cantilever beams with varying lengths was fabricated using a standard surface micro-machining process known as the Multi User MEMS Processes (MUMPs). The purpose of the array was to study the electrostatic actuation mechanisms and the dynamics of the cantilevers. Figure 4.9 shows an SEM image of the cantilever array and Figure 4.10 shows a closer side view of one of the beams. The gap between the beams and the substrate is $2\text{ }\mu\text{m}$. Several vibration measurement techniques were explored to characterize the cantilevers and the following section discusses them with the challenges encountered.

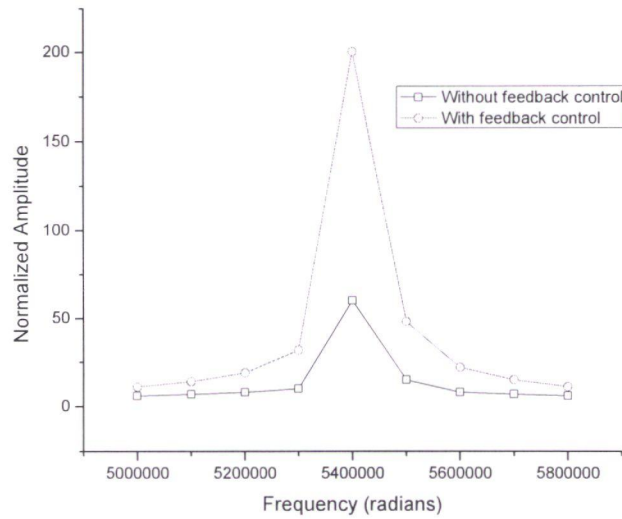


Figure 4.7: Comparison between the uncontrolled and feedback controlled frequency responses.

4.6 Measurement Techniques

This section describes the measurement techniques explored during the course of this research. Static measurements performed by an optical profilometer are first described and then details of different vibration measurement techniques are provided.

4.6.1 Static Measurements

Static deflection measurements are important to characterize the effect of electrostatic force on the cantilever beam displacement. These measurement also allows the extraction of the cantilever beam effective spring constant. The measurements were performed using a Zygo optical profilometer. The main advantage of an optical profilometer for suspended structures is that since it is non-contact, it does not affect the measurements. Potential difference was applied to the cantilever with respect to the substrate and the profilometer image captured for each voltage. The voltage was increased until pull-in occurred. Figure 4.11 shows the cantilever when no voltage was applied and Figure 4.12 shows a shattered cantilever when 40 volts were applied. The voltage was increased

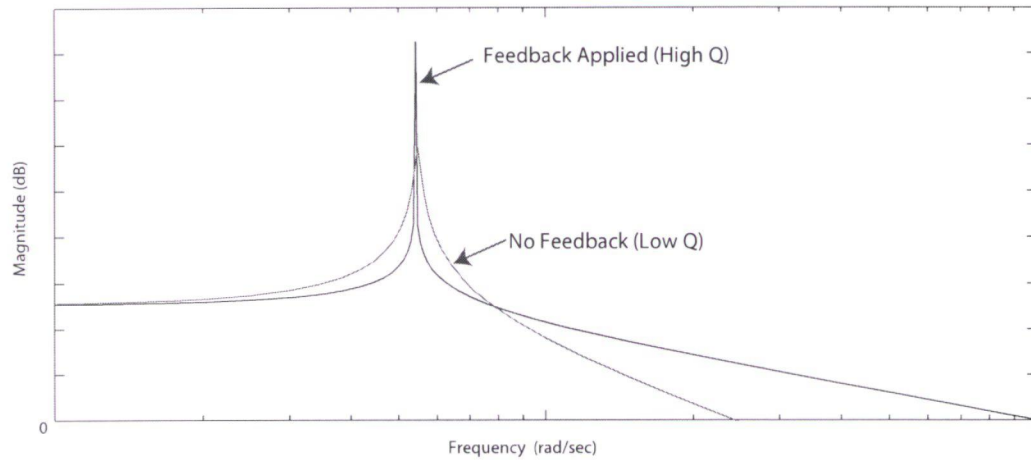


Figure 4.8: Comparison between the uncontrolled and feedback controlled frequency responses using analytical expression of the modified transfer function.

Metal Contact Pad

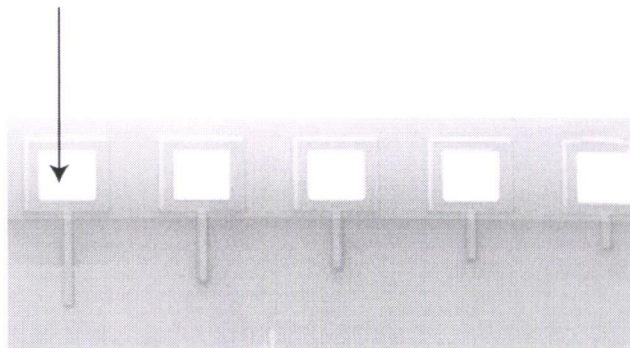


Figure 4.9: An SEM image of an array of cantilever beams fabricated in MUMPs process.

in 2.5V increments, therefore pull-in occurred between 37.5V and 40V. Figure 4.13 shows a comparison between measured results and ANSYS simulation of the beam displacement as a function of voltage. The results are very similar and the difference is probably due to a bump introduced in the cantilevers because of a design error as shown on Figure 4.14. The bump decreases the beam stiffness resulting in more displacement than predicted by ANSYS.

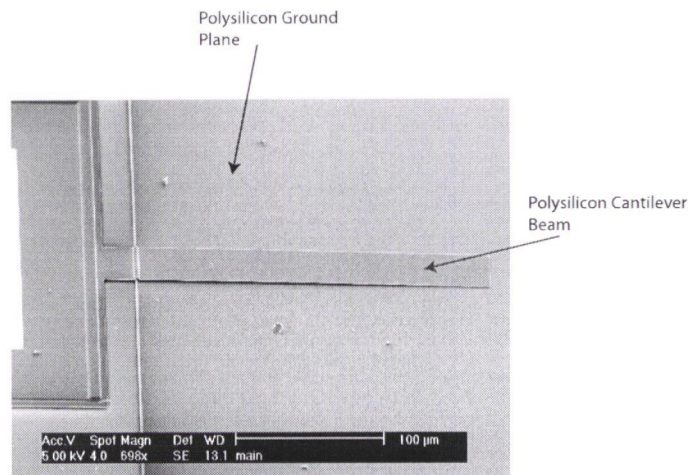


Figure 4.10: An SEM image of side view of one of the cantilever beams.

4.6.2 Vibration Measurements

Models are of limited value unless they are experimentally verified. The reduced order modeling technique based on modal decomposition is a relatively new technique and its applications are limited to a few research groups making it even more important to verify the simulation results. For dynamic MEMS, accurate measurements are usually challenging to perform, and sophisticated measurement techniques are required. This section discusses different measurement techniques that were explored with their advantages and disadvantages.

Capacitive Sensing

Capacitive displacement sensing is the most commonly used technique in MEMS, since it works very well for Silicon and the associated electronics. There are variety of ways to measure displacement by measuring capacitance change, but the one relevant for this work is that of a parallel plate configuration. As described previously and illustrated in Figure 2.5, the cantilever beam and the ground plane are equivalent to a capacitor which depends on the gap. By measuring the change

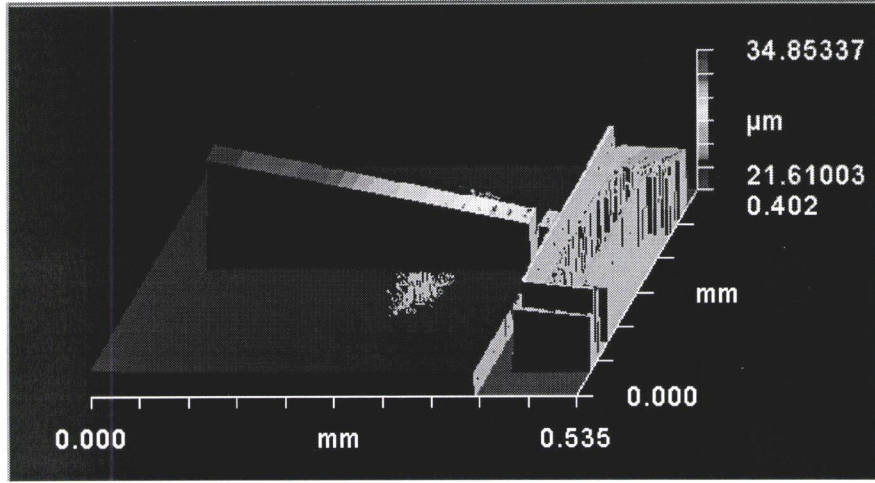


Figure 4.11: A profilometer image of the cantilever beam with no voltage applied.

in capacitance, we can determine by how much the gap has changed. Figure 4.15 shows a capacitance divider configuration where $C(z)$ represents the varying capacitor as the cantilever beam is oscillating and C_{ref} is a fixed reference capacitor. The parasitic capacitance which is out of the designer's control C_p , is shown with a dashed connection.

The impedances of the two capacitors are given as

$$Z(z) = \frac{1}{j\omega C(z)} \quad (4.5)$$

and

$$Z_{ref} = \frac{1}{j\omega C_{ref}} \quad (4.6)$$

By impedance division, the output voltage V_o assuming ideal unity gain buffer, is given by

$$V_o = \left[\frac{Z_{ref}}{Z_{ref} + Z(z)} \right] V_{in} = \left[\frac{\frac{1}{j\omega C_{ref}}}{\frac{1}{j\omega C_{ref}} + \frac{1}{j\omega C(z)}} \right] V_{in} \quad (4.7)$$

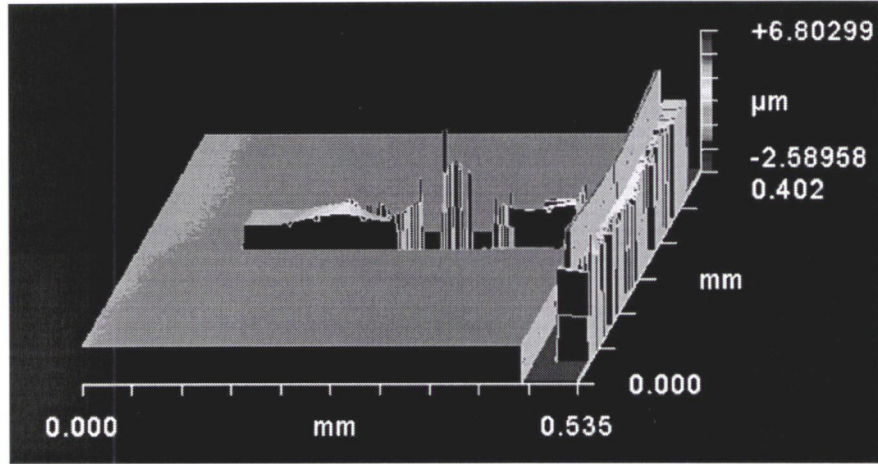


Figure 4.12: A profilometer image of the shattered cantilever beam. The pull-in voltage was found to be around 42V.

Note that we have assumed the parasitic capacitance is negligible. The two capacitances can be expressed as a function of the nominal gap g_0 and displacement z as

$$C(z) = \frac{\epsilon A}{g_0 + z} \quad (4.8)$$

and

$$C_{ref} = \frac{\epsilon A}{g_0} \quad (4.9)$$

Substituting these two values into Equation 4.7 and rearranging, we get

$$V_o = V_{in} \left[\frac{g_0}{2g_0 + z} \right] = \frac{V_{in}}{2} \frac{1}{(1 + z/2g_0)} \quad (4.10)$$

This expression is non-linear, but when the displacement z is small compared to the nominal gap g_0 , it can be linearized to obtain

$$V_o \approx \frac{V_{in}}{2} \left[1 - \frac{z}{2g_0} \right] \quad (4.11)$$

From this equation, the only unknown is the displacement z , which can be determined by measuring V_o . Recently, advances in integrated circuit design have enabled extremely sensitive

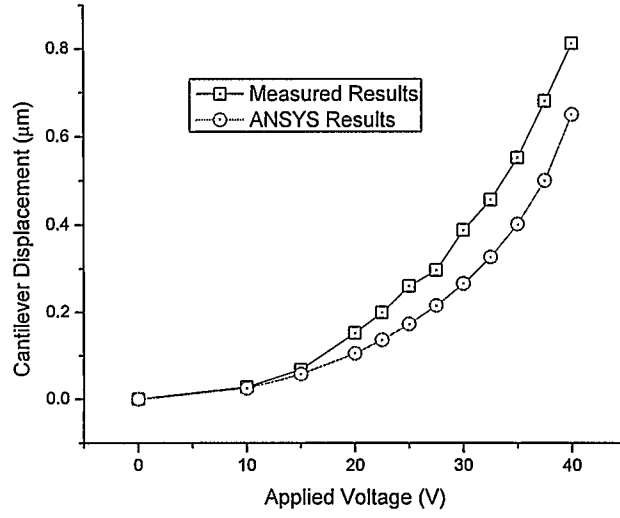


Figure 4.13: Comparison between measured and ANSYS results for electrostatic actuation.

measurements of up to $10 \times 10^{-18} \text{F}$ in capacitance and displacement of up to $10 \times 10^{-15} \text{m}$ [44]. The crucial factor is to ensure that the parasitic capacitance as shown in Figure 4.15, is much less than the measured capacitance, which can only be achieved when the MEMS and the integrated circuit components are manufactured on the same die. If we include C_p , Equation 4.7 becomes

$$V_o = \left[\frac{Z_{ref}}{Z_{ref} + Z(z)} \right] V_{in} = \left[\frac{\frac{1}{j\omega C_{ref}} + \frac{1}{j\omega C_p}}{\frac{1}{j\omega C_{ref}} + \frac{1}{j\omega C(z)} + \frac{1}{j\omega C_p}} \right] V_{in} \quad (4.12)$$

If C_p is very large compared to $C(z)$, we have

$$V_o = V_{in} \left[\frac{1}{1 + C_p/C(z)} \right] \quad (4.13)$$

and the output signal does not vary much when $C(z)$ varies because it is dominated by C_p . For the designed cantilever beams, the largest beam has a nominal capacitance of 5×10^{-14} while the external probes have parasitic capacitance in the range of pico Farads. Hence it is extremely difficult to have accurate measurements with this kind of detection technique unless the sensing electronics are integrated on the same die to minimize the parasitic capacitance. For integrated

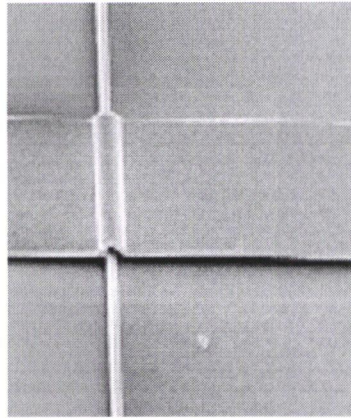


Figure 4.14: A bump close to the fixed end of the beam results in a lower stiffness.

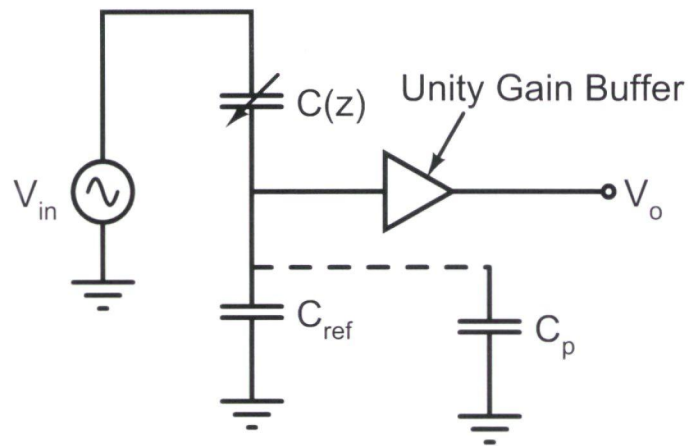


Figure 4.15: A capacitor divider for displacement measurement.

CMOS on the chip, several established capacitance measurement techniques can be used, including chopper stabilized amplifier and correlated double sampling techniques [26]

Atomic Force Microscopy

An atomic force microscope (AFM) is a mechanically based imaging instrument with nanometer resolution. It was invented in 1986 by Binnig and coworkers at the IBM Research Laboratory [45]. The original design consisted of a very compliant cantilever beam with an extremely sharp tip, which has a radius in the order of tens of nanometers. When the tip is brought to close proximity with a surface, the interatomic forces can be measured by determining how much the cantilever

deflects. The deflection was measured by measuring the tunneling current flowing between the surface and a conducting tip.

Over the last fifteen years, vast improvements have been achieved based on this original design. The newer designs utilize optical detection methods for displacement measurement and different modes of operation are available [46]. The most common mode currently in use is the “tapping” mode whereby the cantilever is oscillated on top of the surface. A change in the oscillation amplitude corresponds to a change in the sample profile. This intermittent contact minimizes the contact between the tip and the surface reducing the chance of the surface being damaged and at the same time allowing accurate profiling of soft samples such as biological ones. This mode has also been successfully implemented in fluidic environments enabling the study of biological samples in their native environments.

Referring to Figure 4.16, the AFM cantilever is controlled by a piezoelectric actuator. The actuator allows motion in x , y and z directions. A computer controlled scanner (not shown in the figure), scans the AFM cantilever on the x - y plane over the whole surface of interest. A laser is focused onto the tip of the AFM cantilever and the reflected light is picked up by a position sensitive photo detector. This signal is processed by the computer and using feedback, the distance between the AFM tip and the sample is kept constant over the whole scan. The feedback error signal corresponds to the sample profile.

The experiment as shown in Figure 4.16 was performed using the Bioscope AFM from Digital Instruments with Nanoscope III controller. The sensor cantilever was driven electrostatically which isolates it from the piezoelectric drive of the AFM cantilever. The AFM tip was brought to about 100nm from the vibrating cantilever and the motion of the AFM cantilever recorded. Figure 4.17 shows the recorded signals for two values of electrostatic actuation voltage. The signals were detected only when the frequency of the actuation voltage matches the resonant frequency of the AFM cantilever (272KHz in this case). This indicates very strong coupling between the

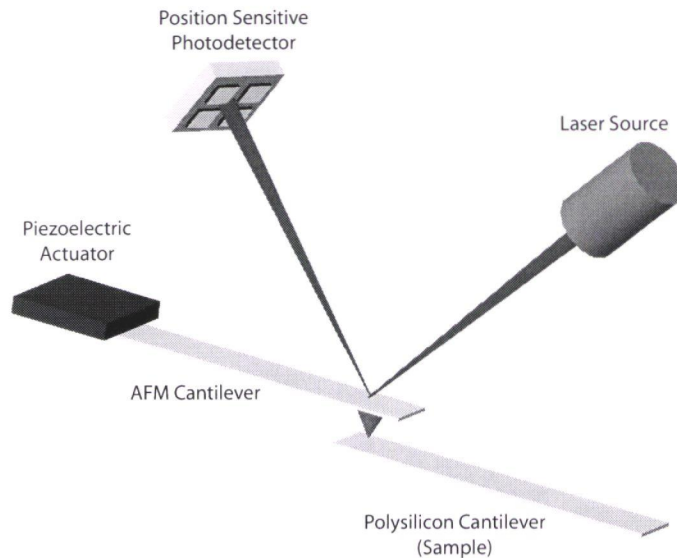


Figure 4.16: The AFM tip track the motion of the sensor cantilever with the displacement detected by a position sensitive photodetector.

two vibrating structures and suggests that it is not possible to measure the motion of the sensor cantilever without affecting it. From the figure, when 1V is applied, the motion is sinusoidal, but at 3V, the signal is clipped at the bottom. This is probably occurring because the AFM tip is hitting the cantilever and the feedback bandwidth does not allow for fast enough response.

From the measurements performed using the AFM, it was concluded that this is not an appropriate method to characterize a vibrating structure for two main reasons:

- The AFM feedback loop bandwidth is too small to accommodate dynamic measurements at typical frequencies.
- The AFM measurement technique is inherently intrusive in a sense that contact, no matter how brief, is made with the dynamic sample and therefore affecting the measurements that we are trying to perform.

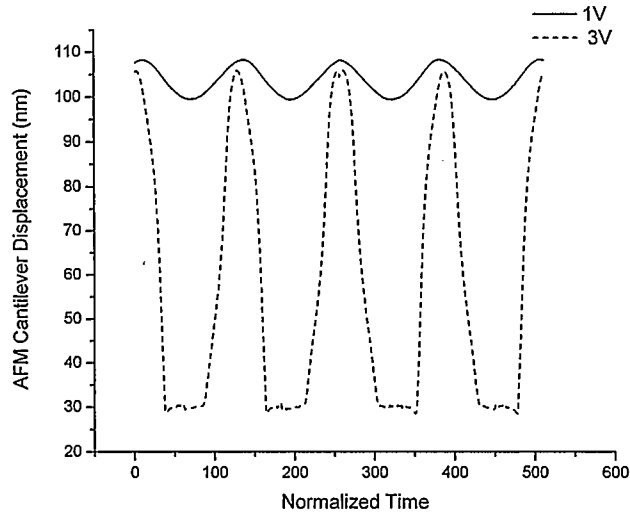


Figure 4.17: Measured results using the Nanoscope III AFM. No output was observed at any frequency other than the resonant frequency of the AFM cantilever indicating strong coupling between the vibrations. The larger amplitude is clipped at the bottom because the AFM cantilever hits on the sensor cantilever.

Optical interferometry, which will be discussed next, is a non-intrusive technique and hence it has a potential to provide more accurate measurements.

Optical Interferometry

The final method for vibration measurement to be discussed in this work is the optical interferometry method. This method is based on analyzing constructive and destructive interference of light waves [47]. Figure 4.18 shows a schematic setup of the system. Light from a He-Ne laser source is split 50/50 into a reference beam and an object beam. The object beam is focused into a cantilever beam free end and the reflected light recombines with the reference beam. As the cantilever beam vibrates, the optical path travelled by the object beam will change, hence modifying the interference pattern at the photo-transistor.

The electric field strength E_r of the reference beam is given by

$$E_r = e^{j\omega_l t} \quad (4.14)$$

where ω_l is the laser frequency. Since the cantilever beam is not a perfect reflector, only a portion of the light will be reflected. Letting the percentage of the reflected light be R , we can write the electric field of the objective beam E_o as

$$E_o = \sqrt{R}e^{j(\omega_l t + \vartheta)} \quad (4.15)$$

where ϑ is the phase difference between the two beams. The square root is due to the fact that light intensity is proportional to the electric field squared. Therefore, the total electric field at the photo-transistor is

$$E_t = e^{j\omega_l t} + \sqrt{R}e^{j(\omega_l t + \vartheta)} \quad (4.16)$$

This can be expressed as

$$E_t = e^{j(\omega_l t + \vartheta/2)}(e^{-j\vartheta/2} + \sqrt{R}e^{j\vartheta/2}) \quad (4.17)$$

Since ω_l is much higher than the bandwidth of the photo-transistor, the term outside the bracket is time averaged and the intensity at the photo-transistor which is proportional to square of the electric field is

$$I \propto |E_t|^2 = E_t(\vartheta) * E_t(-\vartheta) \quad (4.18)$$

This simplifies to

$$I \propto (1 + R) + 2\sqrt{R}\cos \vartheta \quad (4.19)$$

where ϑ is the phase difference between the two interfering beams. If the cantilever has moved by displacement Δz , then ϑ is given by

$$\frac{2\pi}{\lambda} 2\Delta z = 2\kappa \Delta z \quad (4.20)$$

where κ is the optical propagation constant. As the light interferes, it forms fringes with maxima at the locations where there is constructive interferences. this occurs when

$$\Delta z = \frac{\lambda}{2} * n \quad (4.21)$$

where n is an integer. Therefore, by counting the number of fringes, the value of displacement Δz can be determined. This technique is limited by the wavelength of light used. Most laser sources are based on red light with wavelength of $633nm$. Displacement below this value can not be detected since at least one fringe is needed to determine Δz . More sophisticated instruments complement this technique with mixing of optical signals and phase measurements to overcome its weaknesses. One example of an instrument using the mixing (heterodyne) techniques is the Polytec vibrometer with has displacement resolution in the order of picometers.

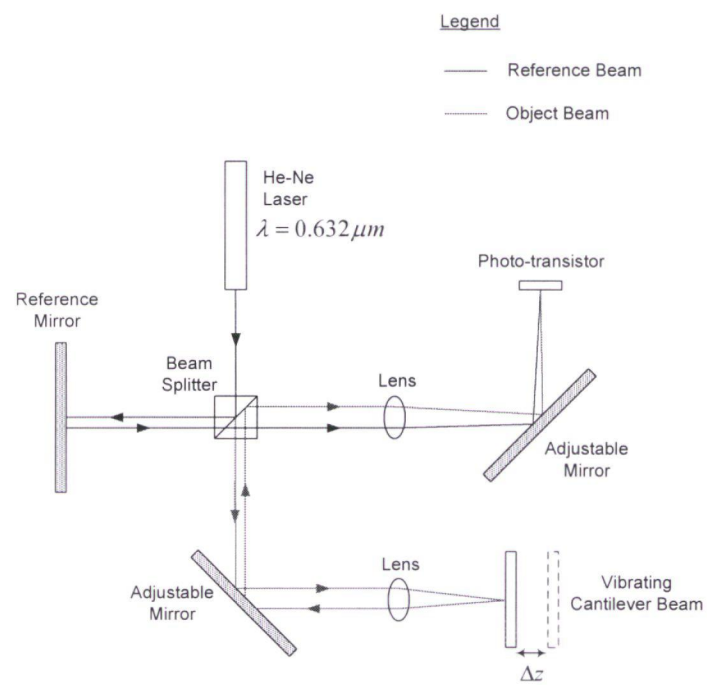


Figure 4.18: Schematic of the interferometer setup to measure vibrations of the MEMS cantilever beam.

Chapter 5

Conclusions

Bio-MEMS has many potential applications, one of them being precise mass measurement for bioparticle detection. Cantilever beams are the simplest structures that can be made using MEMS technology and their frequency shift can be used to accurately measure mass. Even though most dynamic devices operate in their fundamental mode, it was shown that the second mode is better in terms of less damping and also less sensitivity to the bioparticle location on the beam.

The key reason behind the proliferation of microelectronics is the mixture of accurate and easy to use models that can be placed in a system simulator, shielding the system designer from the lower level details. Equivalent models in MEMS are still in their infancy, but once established, they may allow similar widespread use of MEMS sensors and actuators. The reduced order modeling technique is one of the methods with a lot of potential that can be used to represent the dynamics of a transducer in an accurate and compact form.

5.1 Summary of Accomplishments

In this project, design and simulation of a MEMS-based cantilever beam acting as a precise mass sensor in viscous environments were performed. The ROM technique was used to express complex dynamics in a compact form which could be used in system level simulators for performance evaluation as well as designing electronic interfaces to the sensor. The advantages of the ROM technique were also apparent in terms of the speed of execution. By using modal projection technique, damping was calculated for the first two modes of vibration and it was found that the second mode of vibration is less affected by damping. Electrostatic actuation was proposed for driving the cantilever to overcome the thermal noise and coupled domain electrostatic-structural simulation were performed to calculate the displacement of the beam as a function of the voltage applied. The

second mode was also shown to be less sensitive to the position of the mass load on the beam. Since the second mode is at a much higher frequency relative to the fundamental mode, the bandwidth of the sensor is also increased.

5.2 Suggestions for Future Work

Many challenges still remain in the design of the precise mass sensor in viscous environments. The first possible future task is to use the VHDL-AMS code generated by ANSYS in an electronic design environment to create a seamless integration between the transducer and the interface electronics. The code is undocumented and therefore it will take significant effort to make it work properly.

More important is the experimental verification of the models. Sophisticated MEMS characterization equipment with very high resolution, high measurement bandwidth and the ability to perform measurements in fluidic environments is required. Several measurement techniques were explored but they were found to be not suitable for the dynamic characterization of an oscillating beam in viscous environments. Possible techniques include vibrometry, integrated capacitive sensing electronics and integrated optics.

Bibliography

- [1] S. D. Senturia, "Cad challenges for microsensors, microactuators, and microsystems," *Proceedings of the IEEE*, vol. 86, no. 8, pp. 1611–1626, 1998.
- [2] Agilent, "The fundamentals of signal analysis," Tech. Rep. Application Note 243, 2000.
- [3] E. S. Hughes and T. Borst, *Encyclopedia of Computational Mechanics*. John Wiley and Sons, 2004.
- [4] R. Ehrnstrom, "Miniaturization and integration: challenges and breakthroughs in microfluidics," *Lab on a Chip*, vol. 2, no. 2, 2002.
- [5] P. Mitchell, "Microfluidics - downsizing large-scale biology," *Nature Biotechnology*, vol. 19, no. 8, pp. 717–721, 2001.
- [6] M. A. Burns, B. N. Johnson, S. N. Brahmasandra, K. Handique, J. R. Webster, M. Krishnan, T. S. Sammarco, P. M. Man, D. Jones, D. Heldsinger, C. H. Mastrangelo, and D. T. Burke, "An integrated nanoliter dna analysis device," *Science*, vol. 282, no. 5388, pp. 484–487, 1998.
- [7] P. G. Robin Hui Liu, "Development of integrated microfluidic system for genetic analysis," *Journal of Microlithography, Microfabrication and Microsystems*, vol. 2, no. 4, pp. 340–355, 2003.
- [8] Y. L. Li and K. Kaler, "Dielectrophoretic fluidic cell fractionation system," *Analytica Chimica Acta*, vol. 507, no. 1, pp. 151–161, 2004.
- [9] M. A. Schwarz and P. C. Hauser, "Recent developments in detection methods for microfabricated analytical devices," *Lab on a Chip*, vol. 1, no. 1, pp. 1–6, 2001.
- [10] M. Roukes, "Nanoelectromechanical systems face the future," *Physics World*, vol. 14, no. 2, pp. 25–31, 2001.

- [11] G. T. A. Kovacs, N. I. Maluf, and K. E. Petersen, "Bulk micromachining of silicon," *Proceedings of the IEEE*, vol. 86, no. 8, pp. 1536–1551, 1998.
- [12] J. M. Bustillo, R. T. Howe, and R. S. Muller, "Surface micromachining for microelectromechanical systems," *Proceedings of the IEEE*, vol. 86, no. 8, pp. 1552–1574, 1998.
- [13] A. C. R. Grayson, R. S. Shawgo, A. M. Johnson, N. T. Flynn, Y. W. Li, M. J. Cima, and R. Langer, "A biomems review: Mems technology for physiologically integrated devices," *Proceedings of the IEEE*, vol. 92, no. 1, pp. 6–21, 2004.
- [14] S. D. Senturia, "Simulation and design of microsystems: a 10-year perspective," *Sensors and Actuators A-Physical*, vol. 67, no. 1-3, pp. 1–7, 1998.
- [15] H. G. Craighead, "Nanoelectromechanical systems," *Science*, vol. 290, no. 5496, pp. 1532–1535, 2000.
- [16] Z. J. Davis, G. Abadal, O. Kuhn, O. Hansen, F. Grey, and A. Boisen, "Fabrication and characterization of nanoresonating devices for mass detection," *Journal of Vacuum Science and Technology B*, vol. 18, no. 2, pp. 612–616, 2000.
- [17] Z. J. Davis, G. Abadal, B. Helbo, O. Hansen, F. Campabadal, F. Perez-Murano, J. Esteve, E. Figueras, J. Verd, N. Barniol, and A. Boisen, "Monolithic integration of mass sensing nano-cantilevers with cmos circuitry," *Sensors and Actuators A-Physical*, vol. 105, no. 3, pp. 311–319, 2003.
- [18] B. Ilic, D. Czaplewski, H. G. Craighead, P. Neuzil, C. Campagnolo, and C. Batt, "Mechanical resonant immunospecific biological detector," *Applied Physics Letters*, vol. 77, no. 3, pp. 450–452, 2000.
- [19] B. Ilic, D. Czaplewski, M. Zalalutdinov, H. G. Craighead, P. Neuzil, C. Campagnolo, and C. Batt, "Single cell detection with micromechanical oscillators," *Journal of Vacuum Science and Technology B*, vol. 19, no. 6, pp. 2825–2828, 2001.

- [20] J. Mertz, O. Marti, and J. Mlynek, "Regulation of a microcantilever response by force feedback," *Applied Physics Letters*, vol. 62, no. 19, pp. 2344–2346, 1993.
- [21] A. D. L. Humphris, J. Tamayo, and M. J. Miles, "Active quality factor control in liquids for force spectroscopy," *Langmuir*, vol. 16, no. 21, pp. 7891–7894, 2000.
- [22] H. Holscher, "Q-controlled dynamic force spectroscopy," *Surface Science*, vol. 515, no. 2-3, pp. 517–522, 2002.
- [23] J. Tamayo, A. D. L. Humphris, A. M. Malloy, and M. J. Miles, "Chemical sensors and biosensors in liquid environment based on microcantilevers with amplified quality factor," *Ultramicroscopy*, vol. 86, no. 1-2, pp. 167–173, 2001.
- [24] X. M. H. Huang, C. A. Zorman, M. Mehregany, and M. L. Roukes, "Nanodevice motion at microwave frequencies," *Nature*, vol. 421, no. 6922, pp. 496–496, 2003.
- [25] R. W. Clough and J. Penzien, *Dynamics of structures*. McGraw-Hill, 1975.
- [26] S. D. Senturia, *Microsystem design*. Boston: Kluwer Academic Publishers, 2001.
- [27] S. Rast, C. Wattinger, U. Gysin, and E. Meyer, "Dynamics of damped cantilevers," *Review of Scientific Instruments*, vol. 71, no. 7, pp. 2772–2775, 2000.
- [28] B. B. Joseph Seeger, "Parallel-plate driven oscillations and resonant pull-in," in *Solid-State Sensor, Actuator and Microsystems Workshop*, (Hilton Head), pp. 313 – 316, 2002.
- [29] M.-H. Bao, *Micro mechanical transducers : pressure sensors, accelerometers, and gyroscopes*. Handbook of sensors and actuators ; v. 8, Amsterdam New York: Elsevier, 2000.
- [30] M. L. Roukes, "Nanoelectromechanical systems," in *Solid-State Sensor and Actuator Workshop*, (Hilton Head Island, SC), pp. 1–10, 2000.
- [31] R. D. Cook, D. S. Malkus, and M. E. Plesha, *Concepts and applications of finite element analysis*. New York: Wiley, 3rd ed., 1989.

- [32] K.-J. Bathe, *Finite element procedures in engineering analysis*. Englewood Cliffs, N.J.: Prentice-Hall, 1982.
- [33] O. C. Zienkiewicz and R. L. Taylor, *The finite element method*. Oxford ; Boston: Butterworth-Heinemann, 5th ed., 2000.
- [34] S. Moaveni, *Finite element analysis : theory and application with ANSYS*. Upper Saddle River, NJ: Prentice Hall, 2nd ed., 2003.
- [35] J. D. Hoffman, *Numerical methods for engineers and scientists*. New York: Marcel Dekker, 2nd ed., 2001.
- [36] N. Nenadic, *Practical Circuit Models for Piezoelectrically Driven Structures*. Ph.d, University of Rochester, 2001.
- [37] ANSYS, *Multiphysics Simulation for MEMS*. ANSYS Inc., 2002.
- [38] B. S. D. O. Jan E. Mehner, Wolfram Doetzel, "Reduced order modeling of fluid structural interactions in mems based on modal projection techniques," in *12th International Conference on Solid-State Sensors, Actuators and Microsystems.*, vol. 2, (Boston, MA), pp. 1840 – 1843, IEEE, 2003.
- [39] ANSYS, *ANSYS 8.1 Fluid Analysis Guide*. ANSYS Inc., 2003.
- [40] L. D. Gabbay, J. E. Mehner, and S. D. Senturia, "Computer-aided generation of nonlinear reduced-order dynamic macromodels - i: Non-stress-stiffened case," *Journal of Microelectromechanical Systems*, vol. 9, no. 2, pp. 262–269, 2000.
- [41] J. E. Mehner, L. D. Gabbay, and S. D. Senturia, "Computer-aided generation of nonlinear reduced-order dynamic macromodels - ii: Stress-stiffened case," *Journal of Microelectromechanical Systems*, vol. 9, no. 2, pp. 270–278, 2000.
- [42] ANSYS, *ANSYS 8.1 Coupled-Field Analysis Guide*. ANSYS Inc., 2003.

- [43] P. J. Ashenden, G. D. Peterson, and D. A. Teegarden, *The system designer's guide to VHDL-AMS : analog, mixed-signal, and mixed-technology modeling*. Morgan Kaufmann series in systems on silicon, San Francisco, Calif.: Morgan Kaufmann, 2003.
- [44] S. J. C. J. F. Geen, John A.; Sherman, "Single-chip surface micromachined integrated gyroscope with 50 degree/h allan deviation," *IEEE Journal of Solid-State Circuits*, vol. 37, no. 12, pp. 1860 – 1866, 2002.
- [45] G. Binnig, C. F. Quate, and C. Gerber, "Atomic force microscope," *Physical Review Letters*, vol. 56, no. 9, pp. 930–933, 1986.
- [46] R. Garcia and R. Perez, "Dynamic atomic force microscopy methods," *Surface Science Reports*, vol. 47, no. 6-8, pp. 197–301, 2002.
- [47] J. Wylde and T. J. Hubbard, "Measurement of mems displacements and frequencies using laser interferometry," in *Proceedings of the 1999 IEEE Canadian Conference on Electrical and Computer Engineering*, (Edmonton, Alberta), pp. 1680–1685, IEEE, 1999.

Appendix A

VHDL-AMS Code Generated by ANSYS

This appendix lists the VHDL-AMS code generated by ANSYS representing the electrostatically actuated cantilever beam. There are four files, 3 of them containing the initialization parameters, capacitance parameters and strain energy parameters. The fourth file file is the main transducer definition.

A.1 Initialization File

This files defines the package initial which has the constants generated from ANSYS. The variables starting with mm are effective masses for the different modes and the variables starting with dm are the modal damping ratios. The damping ratios are given as 0, but they can be changed accordingly.

```
package initial is

constant mm_1:real:= 0.223506231994E-13;
constant dm_1:real:= 0.000000000000 ;
constant mm_2:real:= 0.221476537857E-13;
constant dm_2:real:= 0.000000000000 ;
constant fil_1:real:= 0.331182713795 ;
constant fil_2:real:= -0.698913064938 ;
constant fi2_1:real:= 0.978390742038 ;
constant fi2_2:real:= 0.977156105566 ;
constant e11_1:real:= -0.351025926171 ;
constant e11_2:real:= 0.192926857049 ;
constant e12_1:real:= 1.53901077348 ;
constant e12_2:real:= -0.838181253949 ;

end;
```

A.2 Capacitance Paramaters

The following file contains the parameters for the capacitance calculations. The parameters will be passed to the main function in the transducer code to generate a polynomial representing the capacitance between the cantilever and the ground plane.

```
package cal2_dat_240 is

constant cal2_type240:integer:=1;
constant cal2_inve240:integer:=2;
signal cal2_ord240:real_vector(1 to 3):=( 2.0 , 4.0 , 0.0 );
signal cal2_fak240:real_vector(1 to 4):=( 0.292660389278 , 11.5720695585,
0.000000000000 , 3101.15257762 );
constant cal2_anz240:integer:= 15;
signal cal2_data240:real_vector(1 to 15):=
(
```

```

    0.793074465996 ,
    0.291438412204 ,
    -0.106893353359 ,
    -0.363298544361E-02,
    -0.730365025174E-02,
    0.765849609438E-02,
    0.797197622947E-03,
    0.500364610441E-03,
    -0.233653987055E-02,
    0.365380095146E-03,
    0.330246939768E-02,
    -0.498895029478E-02,
    -0.188236050626E-03,
    -0.928998245944E-03,
    0.114901269064E-02
);
end;

```

A.3 Strain Energy Parameters

The following file contains the parameters for the strain energy calculations. The parameters will be passed to the main function in the transducer code to generate a polynomial representing the strain energy of the deforming cantilevers for the modes of interest.

```

package s_dat_240 is
constant s_type240:integer:=1;
constant s_inve240:integer:=1;
signal s_ord240:real_vector(1 to 3):=( 2.0 , 4.0 , 0.0 );
signal s_fak240:real_vector(1 to 4):=( 0.292660389278 , 11.5720695585,
0.000000000000 , 3.97244642900 );
constant s_anz240:integer:= 15;
signal s_data240:real_vector(1 to 15):=
(
    0.926530816054E-02,
    0.706073266755E-15,
    0.964655595697 ,
    0.335781004503E-16,
    0.762751070613E-03,
    0.916177302498E-16,
    0.241748221265E-01,
    -0.677353741929E-14,
    0.331926091259E-03,
    -0.199854003675E-16,
    0.148182161168E-04,
    -0.134151750876E-15,
    0.570298802584E-06,
    0.609244341666E-14,
    0.524680812046E-07
);
end;

```

A.4 Transducer

The following is the main transducer entity declaration. The transducer has 8 terminals, 6 of them translational and 2 electrical. The terminals starting with `struc` represents the modal displacement and the terminals starting with `master` represents the nodal displacement (of the master nodes of choice). The bulk of the code is the function *spoly_calc* which generates the capacitance and strain energy polynomials using the arguments from the capacitance and strain energy packages listed above. Once the strain energy and capacitance polynomials are established, the code solves for the terminal related quantities using the ordinary differential equations representing the system dynamics.

```

library IEEE;
use work.s_dat_240.all;
use work.cal2_dat_240.all;
use work.initial.all;
use ieee.electrical_systems.all;
use ieee.mechanical_systems.all;

entity transducer is
  generic (delay:time; el_load1, el_load2:real);
  port (terminal struc1,struc2:translational;
        terminal lagrange1,lagrange2:translational;
        terminal master1,master2:translational;
        terminal elec1,elec2:electrical);
end;

architecture behav of transducer is
  type ret_type is array(1 to 4) of real;

  quantity q1 across fm1 through struc1;
  quantity q2 across fm2 through struc2;
  quantity p1 across r1 through lagrange1;
  quantity p2 across r2 through lagrange2;
  quantity u1 across f1 through master1;
  quantity u2 across f2 through master2;
  quantity v1 across i1 through elec1;
  quantity v2 across i2 through elec2;

  function spoly_calc(qx, qy, qz : in real:=0.0; s_type,s_inve : integer :=0;
                     s_ord, s_fak, s_data:real_vector) return ret_type is

    constant Sx:integer:=integer(s_ord(1))+1;
    constant Sy:integer:=integer(s_ord(2))+1;
    constant Sz:integer:=integer(s_ord(3))+1;
    variable fwx:real_vector(1 to Sx):=(others=>0.0);
    variable fwy:real_vector(1 to Sy):=(others=>0.0);
    variable fwz:real_vector(1 to 1):=(others=>0.0);
    variable dfwx:real_vector(1 to Sx):=(others=>0.0);
    variable dfwy:real_vector(1 to Sy):=(others=>0.0);
    variable dfwz:real_vector(1 to 1):=(others=>0.0);
    variable res_val:ret_type:=(others=>0.0);
    variable fwv,dfwvx,dfwvy,dfwvz,fak2:real:=0.0;
    variable Px_s,Py_s,Px,Py,Lx,Ly,Lz,ii:integer:=0;

```

```

begin
  Lx:=integer(s_ord(1));
  Ly:=integer(s_ord(2));
  Lz:=integer(s_ord(3));
  for i in 1 to Lx+1 loop
    fwx(i):=qx**(i-1)*s_fak(1)**(i-1);
    if i=2 then
      dfwx(i):=s_fak(1)**(i-1);
    end if;
    if i>2 then
      dfwx(i):=real(i-1)*qx**(i-2)*s_fak(1)**(i-1);
    end if;
  end loop;
  for i in 1 to Ly+1 loop
    fwy(i):=qy**(i-1)*s_fak(2)**(i-1);
    if i=2 then
      dfwy(i):=s_fak(2)**(i-1);
    end if;
    if i>2 then
      dfwy(i):=real(i-1)*qy**(i-2)*s_fak(2)**(i-1);
    end if;
  end loop;
  for i in 1 to Lz+1 loop
    fwz(i):=qz**(i-1)*s_fak(3)**(i-1);
    if i=2 then
      dfwz(i):=s_fak(3)**(i-1);
    end if;
    if i>2 then
      dfwz(i):=real(i-1)*qz**(i-2)*s_fak(3)**(i-1);
    end if;
  end loop;
  if s_type=1 then
    ii:=1;
    for zi in 0 to Lz loop
      for yi in 0 to Ly loop
        for xi in 0 to Lx loop
          fwv:=fwv+s_data(ii)*fwx(xi+1)*fwy(yi+1)*fwz(zi+1);
          dfwvx:=dfwvx+s_data(ii)*dfwx(xi+1)*fwy(yi+1)*fwz(zi+1);
          dfwvy:=dfwvy+s_data(ii)*fwx(xi+1)*dfwy(yi+1)*fwz(zi+1);
          dfwvz:=dfwvz+s_data(ii)*fwx(xi+1)*fwy(yi+1)*dfwz(zi+1);
          ii:=ii+1;
        end loop;
      end loop;
    end loop;
  end if;
  if s_type=2 then
    ii:=1;
    Px_s:=integer(s_ord(1));
    Py_s:=integer(s_ord(2));
    for zi in 0 to Lz loop
      Px:=Px_s-zi;
      Py:=Py_s;
      for yi in 0 to Py loop
        for xi in 0 to Px loop
          fwv:=fwv+s_data(ii)*fwx(xi+1)*fwy(yi+1)*fwz(zi+1);
          dfwvx:=dfwvx+s_data(ii)*dfwx(xi+1)*fwy(yi+1)*fwz(zi+1);
          dfwvy:=dfwvy+s_data(ii)*fwx(xi+1)*dfwy(yi+1)*fwz(zi+1);
          dfwvz:=dfwvz+s_data(ii)*fwx(xi+1)*fwy(yi+1)*dfwz(zi+1);

```

```

        ii:=ii+1;
    end loop;
    Px:=Px-1;
end loop;
Py:=Py-1;
end loop;
end if;
if s_type=3 then
    ii:=1;
    for yi in 0 to Ly loop
        for xi in 0 to Lx loop
            fwv:=fwv+s_data(ii)*fwx(xi+1)*fwy(yi+1);
            dfwvx:=dfwvx+s_data(ii)*dfwx(xi+1)*fwy(yi+1);
            dfwvy:=dfwvy+s_data(ii)*fwx(xi+1)*dfwy(yi+1);
            dfwvz:=dfwvz+0.0;
            ii:=ii+1;
        end loop;
    end loop;
    for zi in 1 to Lz loop
        for xi in 0 to Lx loop
            fwv:=fwv+s_data(ii)*fwx(xi+1)*fwz(zi+1);
            dfwvx:=dfwvx+s_data(ii)*dfwx(xi+1)*fwz(zi+1);
            dfwvy:=dfwvy+0.0;
            dfwvz:=dfwvz+s_data(ii)*fwx(xi+1)*dfwz(zi+1);
            ii:=ii+1;
        end loop;
    end loop;
    for zi in 1 to Lz loop
        for yi in 1 to Ly loop
            fwv:=fwv+s_data(ii)*fwy(yi+1)*fwz(zi+1);
            dfwvx:=dfwvx+0.0;
            dfwvy:=dfwvy+s_data(ii)*dfwy(yi+1)*fwz(zi+1);
            dfwvz:=dfwvz+s_data(ii)*fwy(yi+1)*dfwz(zi+1);
            ii:=ii+1;
        end loop;
    end loop;
end if;
if s_type=4 then
    ii:=1;
    Px:=integer(s_ord(1));
    Py:=integer(s_ord(2));
    for yi in 0 to Py loop
        for xi in 0 to Px loop
            fwv:=fwv+s_data(ii)*fwx(xi+1)*fwy(yi+1);
            dfwvx:=dfwvx+s_data(ii)*dfwx(xi+1)*fwy(yi+1);
            dfwvy:=dfwvy+s_data(ii)*fwx(xi+1)*dfwy(yi+1);
            dfwvz:=dfwvz+0.0;
            ii:=ii+1;
        end loop;
        Px:=Px-1;
    end loop;
    Px:=integer(s_ord(1));
    for zi in 1 to Lz loop
        for xi in 0 to Px-1 loop
            fwv:=fwv+s_data(ii)*fwx(xi+1)*fwz(zi+1);
            dfwvx:=dfwvx+s_data(ii)*dfwx(xi+1)*fwz(zi+1);
            dfwvy:=dfwvy+0.0;
            dfwvz:=dfwvz+s_data(ii)*fwx(xi+1)*dfwz(zi+1);

```

```

        ii:=ii+1;
    end loop;
    Px:=Px-1;
end loop;
for zi in 1 to Lz-1 loop
    for yi in 1 to Py-1 loop
        fwv:=fwv+s_data(ii)*fwy(yi+1)*fwz(zi+1);
        dfwvx:=dfwvx+0.0;
        dfwvy:=dfwvy+s_data(ii)*dfwy(yi+1)*fwz(zi+1);
        dfwvz:=dfwvz+s_data(ii)*fwy(yi+1)*dfwz(zi+1);
        ii:=ii+1;
    end loop;
    Py:=Py-1;
end loop;
end if;
if s_inve=1 then
    fwv:=fwv*s_fak(4);
    dfwvx:=dfwvx*s_fak(4);
    dfwvy:=dfwvy*s_fak(4);
    dfwvz:=dfwvz*s_fak(4);
else
    fak2:=1.0/s_fak(4);
    dfwvx:=-dfwvx/(fwv**2);
    dfwvy:=-dfwvy/(fwv**2);
    dfwvz:=-dfwvz/(fwv**2);
    fwv:=1.0/fwv;
    fwv:=fwv*fak2;
    dfwvx:=dfwvx*fak2;
    dfwvy:=dfwvy*fak2;
    dfwvz:=dfwvz*fak2;
end if;
res_val:=(fwv, dfwvx, dfwvy, dfwvz);
return res_val;
end spoly_calc;

signal sene_240:ret_type;
signal cal2_240:ret_type;

begin

p1:process
begin
    sene_240<= spoly_calc(q1,q2,0.0,s_type240,s_inve240,
s_ord240,s_fak240,s_data240);
    cal2_240<= spoly_calc(q1,q2,0.0,cal2_type240,cal2_inve240,
cal2_ord240,cal2_fak240,cal2_data240);
    wait for delay;
end process;

break on sene_240(2), sene_240(3), sene_240(4), cal2_240(2), cal2_240(3),
cal2_240(4);

fm1==mm_1*q1'dot'dot + dm_1*q1'dot +sene_240(2) -cal2_240(2)*
(v1-v2)**2/2.0 +fi1_1*p1+fi2_1*p2 -el1_1*el_load1 -el2_1*el_load2;
fm2==mm_2*q2'dot'dot + dm_2*q2'dot +sene_240(3) -cal2_240(3)*

```



```

(v1-v2)**2/2.0 +fi1_2*p1+fi2_2*p2 -el1_2*el_load1 -el2_2*el_load2;
r1==fi1_1*q1+fi1_2*q2-u1;
r2==fi2_1*q1+fi2_2*q2-u2;
f1==p1;
f2==p2;
i1==+((v1-v2)*(ca12_240(2)*q1'dot+ca12_240(3)*q2'dot)+
(v1'dot-v2'dot)*ca12_240(1));
i2==-((v1-v2)*(ca12_240(2)*q1'dot+ca12_240(3)*q2'dot)+
(v1'dot-v2'dot)*ca12_240(1));

end;

```